Advanced Trigger Development

Thomas H. Jeys, William D. Herzog, John D. Hybl, Richard N. Czerwinski, and Antonio Sanchez

The deadliest form of a biological attack is aerosolized agents dispersed into the atmosphere. Early detection of aerosolized biological agents is important for defense against these agents. Because of the wide range of possible attack scenarios and attack responses, there is also a wide range of detector requirements. This article focuses on real-time, single-particle, optically based bio-agent trigger detectors—the first responder to an aerosol attack—and how to engineer these detectors to achieve optimal detection performance.

Since 1996, Lincoln Laboratory has had an active program in developing state-of-the-art bio-agent sensors [1]. One of the early Lincoln Laboratory successes in biological defense was the development of the Biological Agent Warning Sensor (BAWS) trigger system, which was based on the detection of laser-induced fluorescence from individual aerosol particles. BAWS was conceived and developed from 1996 to 2000. After further development and ruggedization, BAWS was transitioned to the Joint Biological Point Detection System (JBPDS) program. The JBPDS was the first fully automated military bio-agent detection system. In the JBPDS, BAWS performs the trigger function of cueing the air-to-liquid particle collector to begin particle collection for the identifier. Lincoln Laboratory continues to support JBPDS BAWS by developing hardware and software upgrades and testbeds, and by transitioning them to industry. Some examples of this effort are the redesign of the BAWS optical assembly and air flow, the study of additional fluorescence measurement channels, and the modification of the detection algorithm. In addition to the continued BAWS efforts, Lincoln Laboratory is developing more advanced trigger sensors to meet the needs of a wide range of defense applications.

A point-trigger sensor interrogates the ambient atmosphere at a specific geographic point and helps activate other low-disruption actions such as the operation of an identification sensor or the closing or opening of building vents. An example application of a trigger sensor is shown in Figure 1. The role of the trigger is to continuously monitor ambient air for the presence of potential threat aerosols, and if such an aerosol is present to activate the collector and identifier subsystems that then determine whether the aerosol actually contains bio-agents. Present

collector and identifier systems are too costly to operate continuously; thus the main purpose of the trigger system in this architecture is to lower the overall operating costs of the biological detection system. In other sensor architectures, the trigger plays a more active role in the response to a bio-agent attack. As an example, the trigger sensor may be used directly to activate building ventilation controls to protect building occupants. In all applications, the trigger system must detect agent aerosols with high probability at the same time it has a sufficiently low false-trigger rate in operating environments of interest.

There are four related key metrics for evaluating bio-agent detection systems [2]. These are the sensitivity (minimum detectable agent concentration), the probability of detection (at the minimum detectable agent concentration), the false-positive rate, and the response time (the time between the agent concentration reaching the minimum detectable concentration and the sensor detecting the agent). The requirement for each metric depends on the application using the sensor. For example, the detection of a widely dispersed, open-air bio-agent release may require a sensitivity of ten agent-containing particles per liter of air (ACPLA), while the detection of a release inside a building may require only a sensitivity of one thousand ACPLA. Similarly, the acceptable false-positive rate may be once per year for a sensor that will be used to initiate a high disruption response (e.g., building evacuation), while the acceptable false-positive rate may be once per day for a sensor that will be used to initiate a low disruption response (e.g., closing or opening building ventilation ducts). The required detection probability is generally greater than 90% but less than 99%. The required sensor response time in which an attack must be detected strongly depends upon the anticipated response to this detection. For a trigger sensor, the required response time must allow for the anticipated response to agent detection (e.g., collection of aerosol particles for identification, or closing of building vents) and is generally less than 60 seconds. Other attributes (cost, maintenance, reliability, size, weight, and power consumption) of sensors also have a wide range of requirements.

The range of possible sensors is bracketed by a high-performance sensor and a low-cost sensor. For the high-performance sensor, the key metric requirements are of primary importance and the other attribute requirements are of secondary importance. For the low-cost sensor the other attribute requirements (particularly cost) are of primary importance and the key metric requirements are of secondary importance. These two sensor types provide protection for two very different types of bio-agent attacks; a wide-area attack and a point attack. In a wide-area attack the agent is distributed over a wide geographic area (e.g., an entire city) at relatively low concentration. In detecting this type of attack with high probability, the most stressing requirement is the sensitivity of the detector. In this case, a high-performance detector is needed, but because the agent is widely dispersed, not many detectors are needed. In a point attack the agent is distributed over a localized geographic area (e.g., a small fraction of a city or inside a building) at a relatively high concentration. In this case, a low-cost detector is needed because the attack site is not known in advance and thus many detectors must be spread over a wide area in order to obtain a high overall probability of detecting the attack. Since the attack has a locally high agent concentration, the detector need not have high sensitivity. Figure 2 illustrates the application of a high-performance sensor with an array of low-cost sensors.

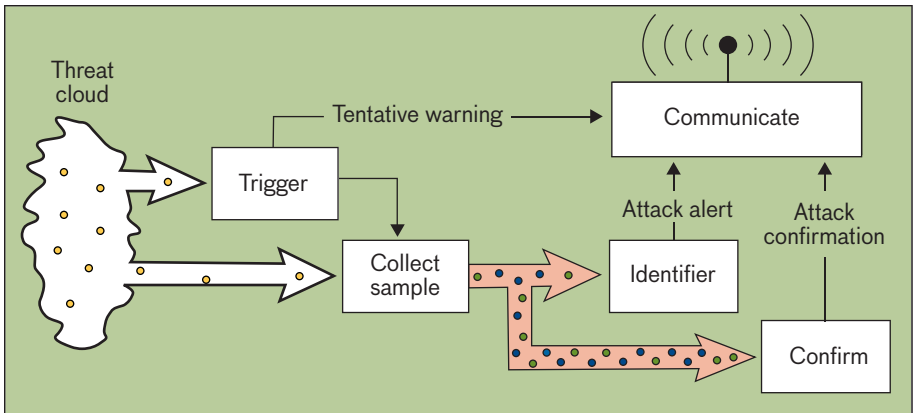

FIGURE 1. The trigger is the first sensor to respond to an aerosol attack. The trigger is continuously analyzing the atmosphere. When it detects a threatening aerosol, it activates the sample collector, which concentrates the aerosol particles (typically into a liquid) for presentation to the identifier. In the event of a positive identification, a further confirmation identification procedure is performed. In each case (trigger, identifier, confirmation), notification and potential actions are initiated.

An important consideration for bio-agent sensors is the environment in which they will operate. Typically, the ambient particle concentration greatly exceeds the desired bio-agent sensitivity. This disparity requires that the sensor be very good at discriminating background particles (clay particles, diesel particles, pollens, molds) from bio-agent particles to achieve a low false-positive rate. For example, in an urban environment the concentration of particles greater than 1 μm diameter may range from 1000 to 100,000 per liter, depending on many parameters (e.g., time of year, traffic conditions). Detecting 100 particles per liter of a similar-sized bio-agent in this environment is like searching for a needle in a haystack.

This article discusses the design and implementation of both high-performance and low-cost real-time single-particle, optically based bio-agent triggers. We introduce the basic concepts of bio-agent detection and describe the optical techniques for the detection and discrimination of bio-agent particles. The component technologies are discussed with several example implementations of bio-agent triggers. We introduce the algorithm process by which the raw data from a sensor are reduced to a binary decision about whether there is or isn't an agent present and conclude with a discussion of the methods by which the key metric requirements of sensors are tested.

Basic Operation of a Bio-Agent Trigger

The detection of bio-agent particles must be done in an ambient background of particles that are in many cases at a much higher concentration than the bio-agent particles. Because of this mismatch in aerosol concentrations, trigger techniques that rely on measurements of the average properties of an ensemble of atmospheric particles are prone to poor discrimination. In this case, a much larger population of normal ambient particles makes discrimination of a small quantity of bio-agent particles difficult. For this reason, we have focused on sensor techniques in which signals from individual particles are measured. More specifically, and because of the desire to detect a bio-agent as rapidly as possible, we utilize optically based particle detection and discrimination techniques. These techniques, which include elastic scattering, auto-fluorescence, and laser-induced breakdown spectroscopy, enable particle discrimination based on a combination of particle features such as size, reflectivity, absorption, fluorescence spectra, and elemental composition.

The design of a real-time, single-particle optically based bio-agent trigger involves two basic considerations. First, individual aerosol particles must be characterized well enough to discriminate between threat and nonthreat particles. Second, the threat-particle concentration must be characterized well enough to support a reliable trigger threshold that maximizes the probability of detection while minimizing false positives. The ability to discriminate different types of particles depends on both the native difference between particle types for the measured properties and the signal-to-noise ratio (SNR) of these measurements. The ability to characterize the threat-particle concentration depends on the detector air sample rate and the time available to make a concentration measurement.

The ability to optically detect and discriminate particles is partially determined by the amount of light that the particle emits. The number of detected photons N_p emitted by a particle, with an optical cross section of σ, which is illuminated by a light beam of wavelength λ with an intensity $I = P/A$ (the light power P in the sample volume divided by the cross-sectional area A of the sample volume) for a time τ is

$$N_P = \eta_c \eta_d \frac{P\tau\lambda}{A\mathrm{hc}}\sigma,$$

The photon collection and detection efficiencies are η_c and η_d, respectively, h is Plank's constant, and c is the speed of light. The number of detected particles n is

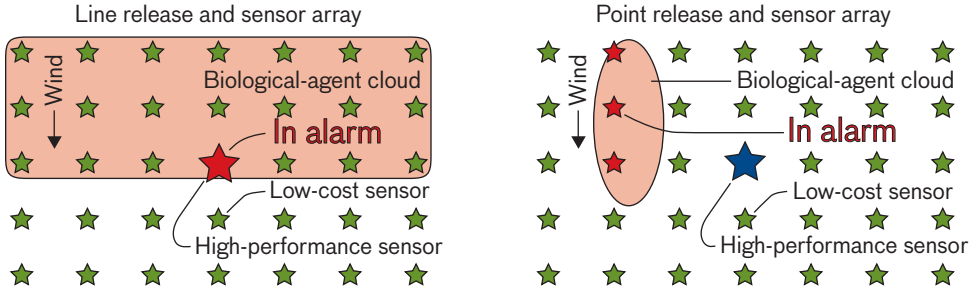

FIGURE 2. Two different types of biological attacks require a combination of high- and low-performance detectors. A wide-area release from a moving source, shown on the left, is best protected by a high-performance sensor, while the localized release shown on the right is best protected by a large array of low-cost sensors.

$$n = \phi CT = \left(\frac{AL}{\tau}\right) CT ,$$

where C is the aerosol particle concentration, T is the time available for counting particles, ϕ is the effective air sample rate (also referred to as responsivity), A is the cross-sectional area of the sample volume, L is the length of the sample volume ($A * L$), and τ is the time required for a particle to transit the sample volume. The SNR is

$$SNR_{\mathrm{p}} = \frac{N_{\mathrm{p}}}{\sqrt{N_{\mathrm{p}} + N_{\mathrm{ca}} + N_{\mathrm{det}}}} ,$$

where N_{p} is the number of detected photons from the particle, N_{ca} corresponds to the number of detected photons in the absence of a particle (i.e., clean air), and N_{det} is the equivalent number of detector noise photons.

Clearly, the number of detected photons is proportional to the power P and thus increasing the power is beneficial. However, the particle cross section and the photon collection and detection efficiencies may be strongly dependent on the source wavelength λ. Each factor must be evaluated together with the others.

The design of a bio-agent detector involves a compromise between maximizing the signal from each particle that enters the sample volume and minimizing the detectable-agent concentration. For a given light power, the maximum particle signal is obtained by focusing that light into the smallest possible cross-sectional area A so as to increase the particle illumination intensity. As the sample volume decreases, however, the minimum detectable concentration increases.

The desired number of detected photons per particle is determined by the desired SNR. Ideally, the SNR should be large enough that photon shot noise does not limit the ability to discriminate threat and nonthreat particles.

Figure 3 illustrates the effects of noise on particle discrimination. If the measurement noise levels are too large it becomes difficult to determine whether a particular particle measurement is indicative of a threat particle. The noise associated with the measurement of particle-emitted photons consists of the shot noise from the particle, the noise coming from gas (e.g., Rayleigh scattering and/or high concentration of very small particles), the noise from structure (e.g., scattering or fluorescence from optical components), and the detector noise.

The magnitude of the particle signal depends on its size. A large particle will generally produce more signal than a small particle. For optical interactions that are confined to the particle surface (e.g., opaque particles) the optical signal depends on the particle surface area and varies as the square of the particle radius. For optical interactions that are uniform throughout the particle (e.g., transparent particles) the optical signal depends on the particle volume and varies as the cube of the particle radius. In general, particles will exhibit both surface and volume interactions, and the relative contribution of these interactions itself depends on particle size. Particles composed of material that is neither opaque nor transparent will behave as a volume for small particles and as a surface for large particles. The particle size below which there is not enough signal to achieve a predetermined SNR is referred to as the particle cut-off size. Because different materials exhibit different levels of optical interactions, the particle cut-off size depends on the particle material. It is desirable to design a bio-agent trigger such that its particle cut-off size is less than the smallest threat particle of interest.

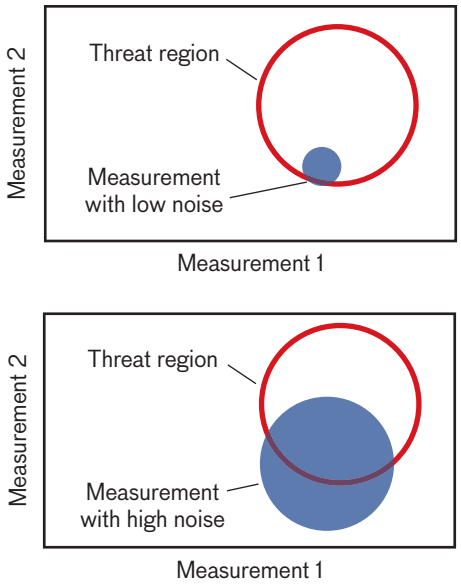

FIGURE 3. Measurement noise affects the ability to discriminate nonthreat-like particles and threat-like particles. The two axes correspond to the magnitude of two different measurements on a single particle. For example, the *x*-axis might correspond to the detected number of elastic-scattering photons and the *y*-axis might correspond to the detected number of fluorescence photons. On the top, a low-noise measurement allows the clear determination that the particle is threat-like, whereas on the bottom, a high-noise measurement confounds the determination of whether this particle is threat-like or a nonthreat-like.

Clutter

It is rarely possible to perfectly discriminate threat particles from nonthreat particles. Typically, there is some small fraction of the background aerosol that resembles the threat particles. These particles are referred to as clutter, and Figure 4 illustrates this concept. In a low-clutter environment the number of threat particles in the measurement threat region dominates the number of clutter particles in the threat region. In a high-clutter environment, the number of clutter particles in the measurement threat region dominates the number of actual threat particles.

For conditions in which the clutter is stationary (the distribution of clutter within the measurement space is fixed), the signal-to-clutter ratio (SCR) for the measured threat particle concentration is

$$SCR_{\text{threat}} = \frac{n_{\text{threat}}}{\sqrt{n_{\text{threat}} + n_{\text{clutter}}}},$$

where n_{total} is the total number of particles detected within the measurement threat region in a time period T and is equal to the sum of the number of threat (n_{threat}) and clutter (n_{clutter}) particles. The threat concentration is then

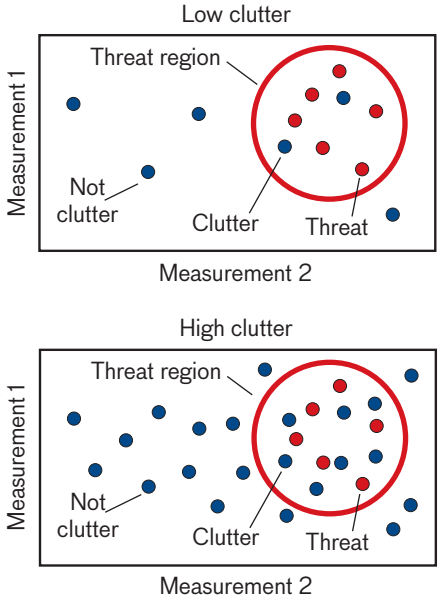

FIGURE 4. Clutter affects the ability of a trigger sensor to discriminate threat particles. Each dot represents a particle and its associated measurements. In this case each has very low noise. The blue dots are nonthreat particles and the red dots are threat particles. The measurement region in which threat particles are expected is shown by the red circle.

$$C_{\text{threat}} = \frac{n_{\text{total}} - n_{\text{clutter}}}{\phi T}.$$

Under stationary clutter conditions it is possible to increase the air sample rate so as to achieve a given SCR for measurement of the threat concentration.

While this clutter analysis is useful for helping to design a trigger sensor in anticipation of a certain clutter concentration, the actual clutter concentration is usually difficult to predict and is often nonstationary. In nonstationary high-clutter conditions, where the desired detectable threat concentration is fixed, there is no substitution for improving or expanding the particle measurements so as to better discriminate particles and thereby reduce the clutter.

Simplified Trigger Detector

Many current bio-agent trigger detectors are based on the detection of induced fluorescence from individual airborne bio-agent particles. Figure 5 shows a simplified optical schematic for such a trigger detector. Light from an ultraviolet (UV)–emitting source of cross-sectional area d^2 is imaged into a sample volume d^3 through which ambient air passes. Particles that pass through the sample volume are illuminated by the UV radiation and re-emit fluorescence radiation. Some of the fluorescence radiation is directed to a photodetector with an area d^2.

We can solve the earlier equations for the detectable bio-agent concentration as a function of the incident optical power. The light-beam cross-sectional area (A or d^2), the particle transit time τ through the sample volume, and the air sample rate have dropped out of the equations, leaving

$$C = \frac{n}{\sigma L T}\frac{N_{\text{p}}}{\eta_{\text{c}}\eta_{\text{d}}}\frac{\text{hc}}{P\lambda}.$$

Figure 6 shows the detectable concentration as a function of optical power for an SNR of 10 and for illumination wavelengths of 280 nm and 340 nm.

Optical Detection of Bio-Agent Particles

A wide variety of optical phenomena have been investigated for the detection of bio-agents. However, for single-particle detection, only elastic scattering, fluorescence, and, recently, laser-induced breakdown spectroscopy (LIBS) have been developed to the point of field demonstrations of bioparticle detection. (While vibrational spec-

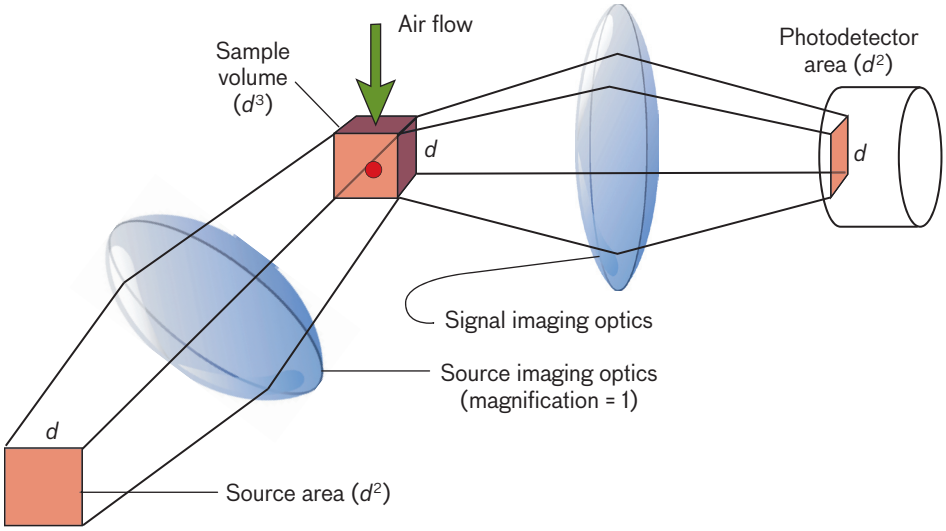

FIGURE 5. A generic individual airborne bioparticle detector consists of a source, imaging optics, a detector, and the sample region.

troscopy can provide good discrimination capability, its accompanying very small optical cross section has, to date, prevented rapid detection and discrimination of aerosolized single-particle [1 to 10 μm diameter] bio-agents or simulants.) These phenomena greatly differ in terms of signal strength and particle discrimination. Elastic scattering generates large signal strengths but has few features for discriminating particles made of different materials. Fluorescence generates much smaller signals but has several features for discriminating different types of particles. LIBS generates large signals and has many features for discriminating particles. The combination of these phenomena increases the ability to discriminate particles.

Elastic Scattering

The elastic scattering of electromagnetic radiation is a process in which the scattered (or reflected) radiation has the same wavelength as the incident radiation (see Figures 7 and 8). Elastic scattering from an aerosol particle has a large cross section compared with other possible optical interactions. A large cross section results in large-measurement signal strength. Depending on the ratio of particle size to wavelength of incident radiation, the elastic-scattering process can be divided into three regimes; Rayleigh scattering, Mie scattering, and geometric scattering. Rayleigh scattering [3] occurs whenever the particle size is much less than the radiation wavelength (e.g., visible-wavelength scattering from air molecules). Geometric scattering occurs whenever the particle size is much greater than the radiation wavelength (e.g., visible-wavelength scattering from rain drops). For geometric scattering the scattering cross section is comparable to the cross-sectional area of the particle. While the Mie scattering theory [4] is valid for all particle sizes and wavelengths, it is typically used only whenever Rayleigh scattering or geometric scattering theory is not appropriate (e.g., when the wavelength and particle size are

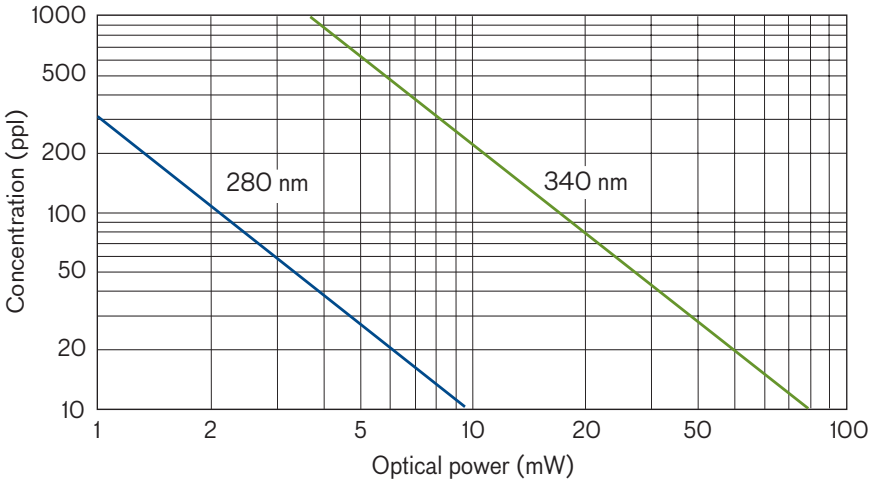

FIGURE 6. The calculated detectable-particle concentration for light-induced fluorescence is a function of the optical power and the illumination wavelength. The primary factor separating the two lines is the particle fluorescence cross section (σ). This value is 50×10^{-12} cm^2 for 280 nm fluorescence and only 5×10^{-12} cm^2 for 340 nm fluorescence. Other parameters used for this calculation were the number of detected particles (n = 100), the number of detected photons (N_p = 100), the photon collection and detection efficiencies (η_c = 30%, η_d = 15%), the threat detection time (T = 60 sec), and a sample transit time (τ = 1 msec). For this figure, we did not include clean air, detector noise, or clutter.

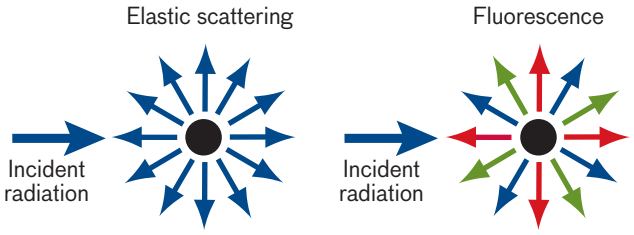

FIGURE 7. In elastic scattering, some of the incident radiation promptly scatters (or reflects) from a particle such that the scattered wavelength is identical to the incident wavelength. In particle fluorescence, some of the incident radiation is absorbed by the particle and is later re-emitted by spontaneous emission. In complex molecular systems the spontaneous emission usually occurs at longer wavelengths.

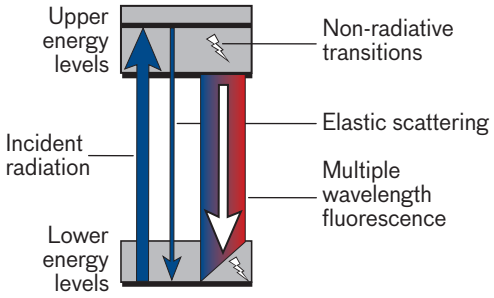

FIGURE 8. Illustration of elastic scattering and fluorescence between two molecular energy bands. The elastic scattering results from excitation and emission of radiation from the same molecular energy levels. Fluorescence results from excitation of an upper energy level and relaxation of the molecule to the lower edge of the upper energy band followed by spontaneous emission of radiation as the molecule transitions from the lower level of the upper energy band to a range of energy levels in the lower energy band. The result is a spectrum of wavelengths.

within a factor of about 10 of each other). Mie scattering accounts for the interference of radiation from different portions of the particle and results in highly structured angular scattering patterns (see Figure 9). The Mie-scattering angular pattern is very dependent on the particle size and shape.

The elastic scattering of radiation from an aerosol particle is caused by a difference in the index of refraction of the particle and the medium in which it resides (air). The index of refraction can be expressed as a complex number ($n = n_r - i\,n_i$). The real part of the index (n_r) is given by the ratio of the radiation propagation speeds in a vacuum and in the medium of interest. The imaginary part of the index (n_i) is related to the absorption of incident radiation. A particle with an index equal to that of the medium in which it resides (e.g., $n = 1$ for air) will not scatter any of the incident radiation. A particle with a diameter comparable to, or larger than, the wavelength of the incident radiation and with a large real index will scatter a large fraction of the incident radiation, while a similarly sized particle with a large imaginary index will absorb a large fraction of the incident radiation in addition to scattering part of the radiation.

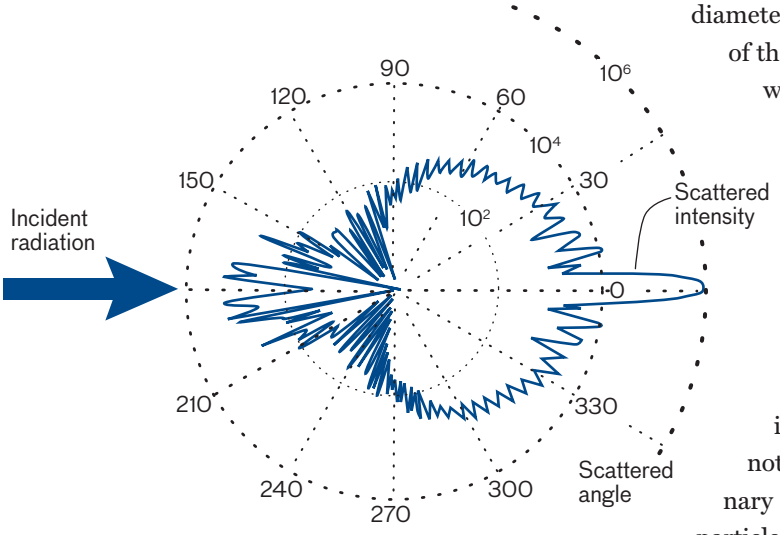

FIGURE 9. Mie scattering exhibits a highly structured angular scattering profile, as shown in this example for 300 nm radiation from a 2 μm diameter spherical and homogeneous particle with a refractive index of n = 1.5. The incident radiation travels from left to right in the diagram. The logarithm of the magnitude of the scattered radiation is given by the radial distance on the polar plot. The outer circle corresponds to a relative scattering magnitude of 10^6, while the inner circle corresponds to a relative magnitude of 10^2.

For a particle with an index of refraction different from the medium in which it resides, the amount of radiation scattered, the angular distribution of the scattering, and the polarization characteristics of the scattering depend not only on the magnitudes of the real and imaginary parts of the index of refraction but also on the particle size, shape, orientation, and wavelength of the incident radiation. Elastic scattering is commonly used to measure particle size [5] and has also been used to measure particle shape [6–8]. While particle size and shape can be used to augment bio-aerosol detection schemes, they do not provide much information about the chemical or biological nature of aerosol particles and are therefore limited in their discrimination capability. These

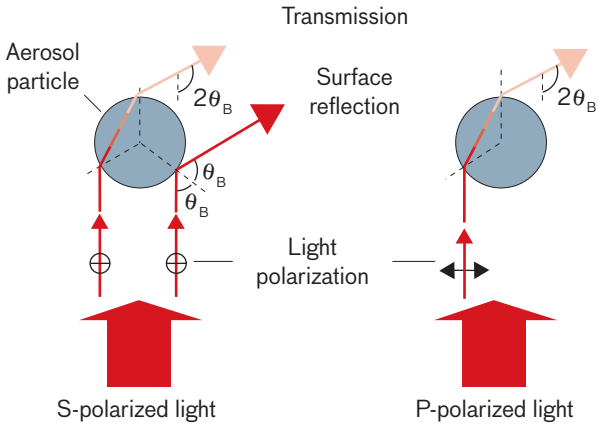

FIGURE 10. Ray tracing of the optical paths shows the distinction between S-polarized and P-polarized scattering from a dielectric sphere. For light incident at Brewster's angle, θ_B, S-polarized light experiences both reflection and refraction from the particle surface. P-polarized light, however, experiences refraction only at the particle surface. After refraction at the surface, the P-polarized light propagates through the particle and refracts at the interface on the opposite side of the particle before scattering into the far field.

methods to access the information contained in the refractive index, particularly the imaginary part of the index, are of significant interest for high-discrimination sensing. Disentangling all the properties responsible for the elastic scattering signal for a given particle in order to ascertain its refractive index is difficult. However, several scattering-based techniques have been developed to access this information [9, 10]. Of these, Brewster-angle scattering, described below, has been shown to be useful in discriminating highly absorbing particles such as soot from bio-agent stimulant particles.

Brewster-angle elastic scattering can determine the relative amount of particle absorption through the measurement of the ratio of scattered S-polarized light (polarized perpendicular to the plane of scattering) and scattered P-polarized light (polarized in the plane of scattering). The S-polarized scattering is relatively insensitive to the particle absorption because it consists mostly of light that is scattered from the particle's surface, while the P-polarized scattering is strongly dependent on particle absorption because the light has propagated through the particle. This effect is illustrated in Figure 10.

Figure 11 shows experimentally measured histograms of the ratio of the P-polarized to S-polarized scattering for 2 μm polystyrene spheres, diesel exhaust particles, *Bacillus globigii* (*Bg*) spores, and ovalbumin (Ov) that ranged in size from 1 to 5 μm. The diesel particles exhibit significant extinction of the P-polarized light relative to S-polarized light.

Fluorescence

Fluorescence is a process in which some of the incident radiation is absorbed by the particle and is then later re-emitted as spontaneous emission [11]. In complex molecular systems the spontaneous emission usually occurs at longer wavelengths than the incident radiation. The absorption spectrum, emission spectrum, and magnitude of particle fluorescence are strongly dependent on the composition of the particle. All biological organisms emit fluorescence when illuminated by ultraviolet light. For clean organisms, this fluorescence can be primarily attributed to the biochemicals, tryptophan and tyrosine (amino acids), nicotinamide adenine dinucleotide (NADH), and riboflavin. However, often organisms are coated with other materials, such as growth material, that can significantly change the particle fluorescence strength and spectrum.

Measurement of the fluorescence properties of individual aerosol particles can provide broad discrimination between bio-agents and atmospheric background aerosols. Fluorescence cross sections for bio-aerosols are roughly 10^3 to 10^5 less than the corresponding elastic-scattering cross sections. The greatly reduced cross-

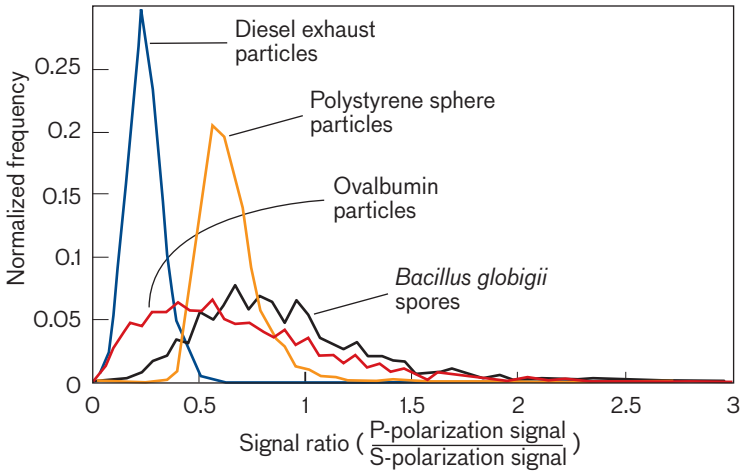

FIGURE 11. Histograms of P-to-S polarization signal ratios show significant differences between diesel, polystyrene, ovalbumin (Ov), and *Bacillus globigii* (*Bg*) aerosol particles.

section requires fluorescence-based sensors to utilize higher-power optical sources, more sensitive photodetectors, and optical systems that are more efficient at collection of the particle signal, relative to elastic-scattering-based sensors.

The success of fluorescence-based bio-aerosol sensors [12–19] is due in part to the relatively low concentration of fluorescent particles in the air. On the basis of our measurements, we found that less than 20% of particles in the 1 to 10 μm size range are significantly fluorescent. However, the fraction of fluorescent particles fluctuates significantly, depending upon geographic location, season, and time of day. In desert environments the fraction will be low (e.g., 1%), while in urban environments the fraction will be comparatively high (e.g., 10%). In addition to discrimination based simply upon whether or not a particle fluoresces, other properties such as the emission spectrum, fluorescence lifetime, and response to different excitation wavelengths can be used to enhance the discrimination of threat and nonthreat particles.

The fluorescence excitation emission spectrum of various bio-agent simulants and common atmospheric particles has been measured by multiple organizations [20–24]. Figure 12 shows the relative fluorescence cross section for tryptophan, NADH, and riboflavin, when irradiated by 280 nm, 340 nm, and 450 nm sources, respectively. Each of these materials was irradiated with a source that was close to the peak absorption of the material. Figure 13 shows the normalized emission spectra of several bio-agent simulants. One issue that significantly affects the highly specific fluorescence signatures (e.g., temporal, spectral) for biodetection is the variability of the bio-agents. The detailed fluorescence properties of a particular bio-agent can change dramatically, depending on the method in which it was grown, stored, or disseminated, as shown in Figure 13. Figure 14 shows false-color images of the excitation and emission spectra of several materials. Except for the pure chemicals (tryptophan, NADH, riboflavin, Ov) these spectra are very dependent on other materials that accompany the material of interest. The *Bg* spectra show a wide variation due to the preparation method.

Laser-Induced Breakdown Spectroscopy

Biological organisms contain a wide variety of inorganic elements such as calcium, magnesium, manganese, iron, phosphorus, sodium, potassium, and silicon. In some cases, the relative amounts of these elements vary between different classes of organisms. For example, it is well known that during sporulation, bacterial spores concentrate calcium dipicolinate [25], which suggests that elemental analysis may offer the potential for broad classification of bio-aerosols. Table 1 shows the elemental composition of four different biological samples and the ability to distinguish *Bg* from the fungal spores on the basis of elemental composition (especially calcium).

Several techniques exist in atomic spectroscopy for the elemental analysis of laboratory samples. However, many of these techniques are not easily translatable into field instruments. Laser-Induced Breakdown Spectroscopy (LIBS) [26–33] is one of the most practical means for bringing elemental analysis to the field. As illustrated in Figure 15, LIBS involves tightly focusing a pulse of laser light in order to generate electric field strengths sufficient for plasma creation. Material inside the plasma volume is ionized and decomposed into atomic constituents. The hot plasma (10,000 to 15,000 K) provides a thermal excitation source for the atomized species within the plasma volume. Emission from these electronically excited atoms and ions is spectrally resolved and used to determine the elemental composition of the sample.

Figure 16 displays LIBS spectra for various bio-agent simulants and other atmospheric background materials. Visual inspection of the individual LIBS spectra reveals that each class of biological sample has a distinctive feature: calcium-to-potassium ratio much greater than

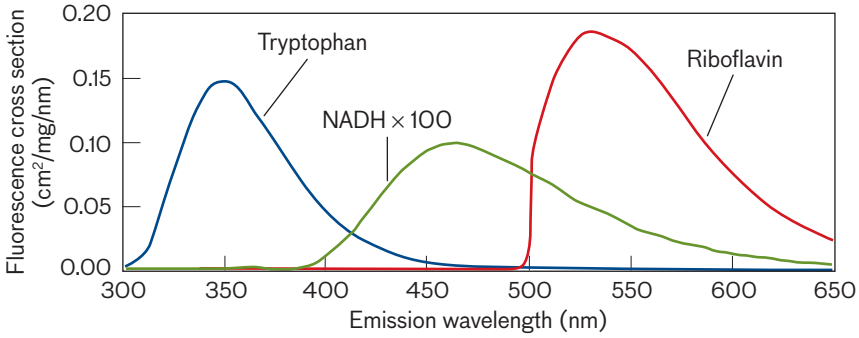

FIGURE 12. The fluorescence cross sections for tryptophan, nicotinamide adenine dinucleotide (NADH), and riboflavin are broad functions of emission wavelength for excitation at 280 nm, 340 nm, and 450 nm, respectively.

one in *Bg*, calcium-to-potassium ratio much less than one for fungal spores (e.g., *penicillium*), an overwhelming sodium signal in the *Ov* spectrum, and a minimal sodium signal (combined with a calcium-to-potassium ratio greater than one) in pollen. In most of the biological samples a relatively broad peak is seen around 387 nm, attributed to recombination of cyanide in the cooling plasma. Potentially, this molecular peak could be used to separate predominantly carbon-based particles (mostly biological) from inorganic particles.

Table 1: Elemental Analysis of Biological Samples

ELEMENT	*BACILLUS GLOBIGII* SPORES	FUNGAL SPORES OAT SMUT	FUNGAL SPORES WHEAT SMUT	FUNGAL SPORES CORN SMUT
Ca	1.16	0.16	0.0147	0.12
Mg	0.30	0.20	0.0937	0.19
Na	0.45	0.0132	0.0110	0.0171
K	0.49	1.60	2.24	1.63
Fe	0.67	0.0253	0.0032	0.0081
P	2.30	0.44	0.41	0.58
Mn	0.0081	0.006	0.0024	0.0037

Elemental concentrations are given as percent by weight

Single-particle LIBS analysis of biological aerosols requires operating near the technique's detection limit. This task is difficult because variations in plasma properties limit the reproducibility of measured elemental ratios to approximately 10% to 25%. However, single-particle analysis is necessitated because of the ubiquity of such elements as calcium, sodium, potassium, and magnesium in the environment. Single-particle analysis provides the ability to segregate particles into distinct populations by exploiting the full correlation of the fluorescence and elemental signatures of each particle. As with fluorescence, LIBS signatures can change dramatically with preparation and handling methods. Therefore, it is important to generate broad, encompassing signatures and to combine LIBS analysis with techniques such as fluorescence that provide orthogonal information.

Trigger Implementation

An optically based bio-agent trigger system requires an air delivery subsystem, a particle illumination subsystem, and a particle signal-detection subsystem. These subsystems are conceptually illustrated in Figure 5. The air delivery subsystem is responsible for taking outside ambient air into the trigger housing and passing this air through the sample volume. In addition to this primary task the air delivery subsystem may also concentrate the particle

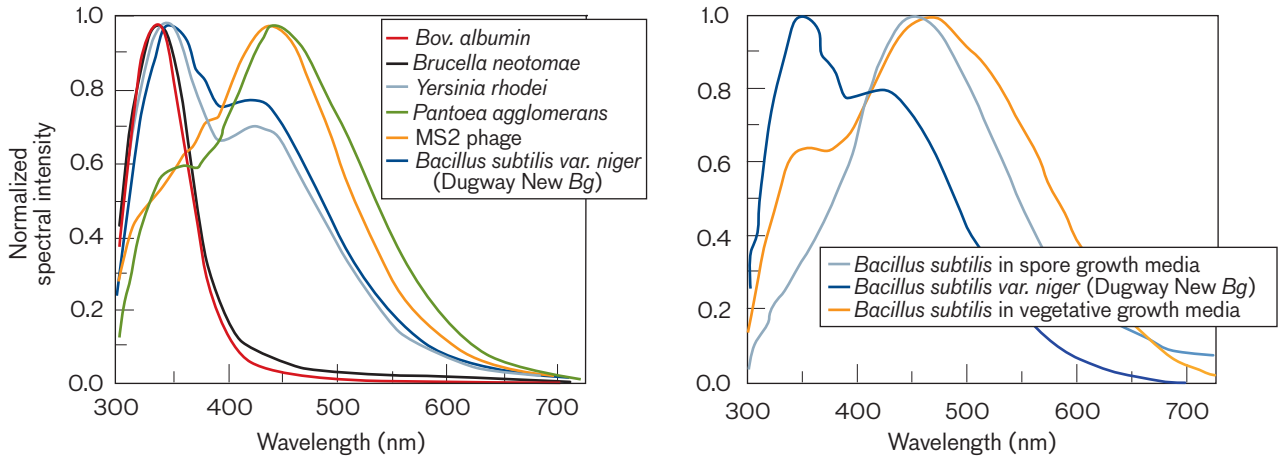

FIGURE 13. As in Figure 12, in which the incident radiation wavelength is changed, here the emission wavelengths vary on the basis of the material. On the left are the normalized spectral intensities as a function of emission wavelength for various biological materials excited by 266 nm radiation. On the right are the normalized spectral intensities for the same material (*Bacillus subtilis* [*Bs*]) in several configurations, also excited by 266 nm radiation.

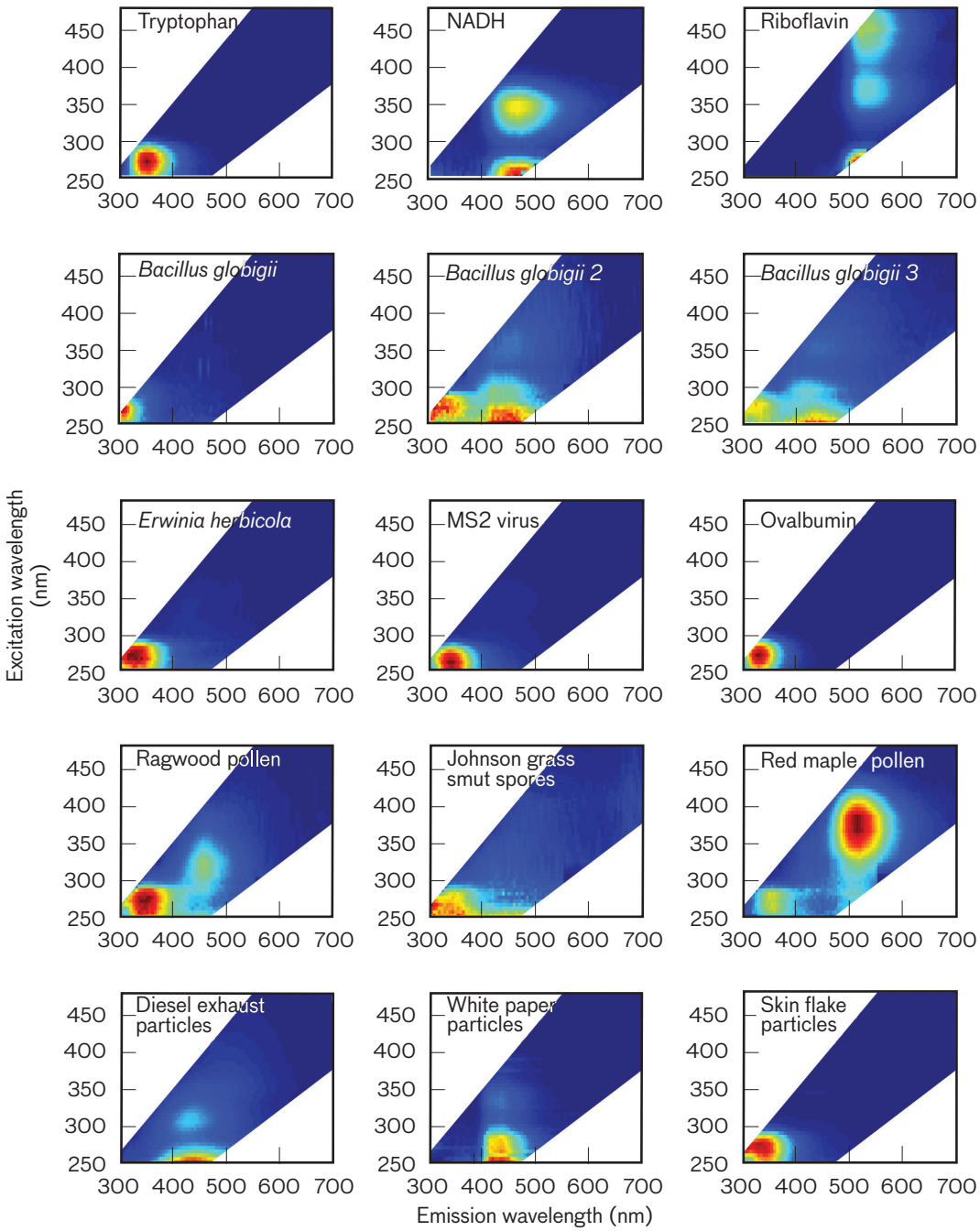

FIGURE 14. Distinctive signatures are observed when the fluorescence excitation-emission spectra are plotted. For each plot of the various biochemicals, bioparticles, and other particles, the relative magnitude of the fluorescence is given in false color: deep red for strong fluorescence and deep blue for no fluorescence.

number density (e.g., virtual impaction) or it may keep the trigger optics clean from contamination by outside air (e.g., sheath air flow). In some trigger systems the transit time of the particle across the sample flow needs to be well controlled; thus laminar airflow may be required.

The particle illumination subsystem is composed of one or more light sources (e.g., laser, LED) and optical components for efficiently transporting the light to the sample volume with the correct cross-sectional shape and, if it matters, the correct polarization. The particle signal-detection subsystem is composed of optics for efficiently collecting the radiation emitted by a particle in the sample

volume and delivering this radiation to one or more photodetectors. Both the illumination optics and the particle detection optics should be designed to maximize the amount of particle radiation incident on the photodetector at the same time minimizing the amount of non-particle radiation that is incident on the photodetectors. Depending on the details of the trigger operation and the desired particle measurements (e.g., elastic scattering or fluorescence), the light sources may be continuous or pulsed and may be composed of a single or multiple radiation wavelengths. In general, higher optical power and higher optical intensity in the sample volume make particle detection easier. However, often space and electrical power constraints limit the available optical power and intensity. The photodetector shown in Figure 5 may be composed of multiple detectors for measuring the wavelength resolution, temporal resolution, or polarization of the particle signal. The photodetector(s) must detect the particle radiation with a sufficient SNR for discrimination between particle types. Often the particle signal is low, and thus sensitive and low-noise photodetectors must be used. In addition, the cross-sectional area of the sample volume, from which particle light may originate, along with low-magnification optics in a compact housing often dictates that the photodetector has a relatively large sensitive area.

Trigger implementations may involve the use of one or more optical sources. If only one source is used, that source must be either continuous wave (CW) or pulsed at a high enough repetition rate so that the air sample rate is sufficient for the detection of threat concentrations of interest. If more that one source is used, one source is usually CW (such as a near-infrared diode laser), and the elastic-scattering signal from a transiting particle provides timing information with which to cue the other sources. These other sources need not be as efficient, because they are used only when a particle is known to be present.

Photodetectors

The utility of a photodetector is determined by many features, including the sensitivity at the wavelengths of interest, dark and read noise, size of sensitive area, size of photodetector housing, required electrical input, and cost. The photomultiplier tube (PMT) [34] is a near-ideal photon detector with a small dark-count rate (<10 kHz/cm^2 at room temperature), and a good photon detection efficiency (0.12 to 0.30). In addition, the PMT can have a conveniently large (~1 cm^2) photon collection area. However, the PMT is relatively fragile and requires high voltage (~1 kV). In contrast, semiconductor-based photodetectors are more robust, smaller, and generally less expensive than PMTs.

Among semiconductor-based photodetectors, silicon is the most attractive material because it is sensitive in all wavelength bands of interest (UV through visible), it is robust, it does not require high voltages, and it is the basis for low-cost detectors and imagers in the consumer electronics market. Unfortunately, silicon detectors have a high detector-noise-per-unit active area compared to PMTs. Silicon detectors therefore require the use of small active areas and optical systems that efficiently gather the particle signals and focus this signal onto the small active area. Arrays of detectors that each sample different small portions of the sample volume can be used to avoid expensive optical systems that must efficiently gather signal photons from a large sample volume and focus these photons onto a small detector area. Candidate detector arrays are found among imaging arrays, currently used for 3-D imaging lidars (Geiger-mode APDs), and low-cost consumer electronics imagers (e.g., charge-coupled devices [CCD]).

Figure 17 shows the bio-agent, fluorescence-detection performance

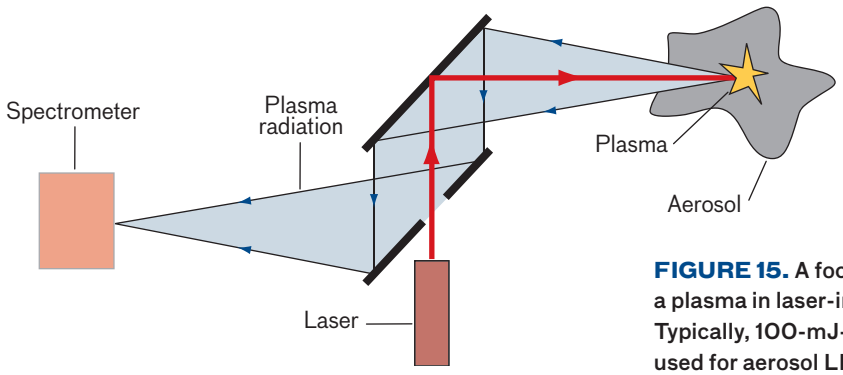

FIGURE 15. A focused laser pulse hits an aerosol and creates a plasma in laser-induced breakdown spectroscopy (LIBS). Typically, 100-mJ-class pulsed Nd:YAG lasers (1064 nm) are used for aerosol LIBS to generate the 10 to 100 GW/cm^2 intensities that are needed to initiate an air plasma.

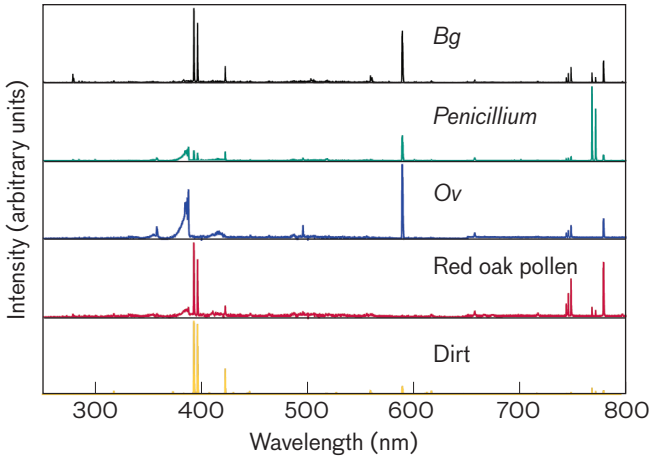

FIGURE 16. Representative LIBS spectra of bio-agent simulants and background materials show the effective discrimination of the LIBS technique. Each spectrum is an average of 50 to 100 laser pulses. The prominent atomic lines are magnesium (Mg ~285 nm), calcium (Ca 393, 396, and 422.7 nm), sodium (Na ~589 nm), and potassium (K ~766 nm). Approximate wavelengths are given, since some are unresolved or partially resolved multiplets. Molecular cyanide appears as a broad peak around 387 nm in some of the spectra. Atmospheric nitrogen (N) is visible at roughly 741, 743, and 746 nm, and a prominent oxygen (O) line is apparent at 777 nm.

for several silicon-based photodetectors as well as the PMT. The minimum detectable concentration is given as a function of the particle size. These performance curves were generated by assuming a fixed excitation wavelength (340 nm), a fixed particle illumination intensity (0.33 W/cm^2), a fixed particle transit time (1 ms) of the sample volume, a fixed overall detector size (5 mm × 5 mm), the detection of 100 particles per minute, and a specific relation between the particle diameter and the particle fluorescence cross section ($\sigma = 5 \times 10^{-12}\, r^{2.5}$ cm^2 [35], where r is the particle diameter in μm). Each detector is assumed to be composed of an array of sub-elements that are imaged with unity magnification into the sample volume. The depth of field of each sub-element is assumed to be equal to the dimension of the sub-element. Thus, for example, a 0.5 mm × 0.5 mm detector sub-element is assumed to be sensitive to particle signals from a sample volume of 0.5 mm × 0.5 mm × 0.5 mm, and the total detector is assumed to be sensitive to particle signals from a sample volume of 5 mm × 5 mm × 0.5 mm. Clearly, the largest sample volume, and hence the lowest detectable concentration, is obtained by utilizing the largest possible sub-element size. However, in most cases the detector noise increases linearly with the sub-element area. The sub-element sizes were appropriately adjusted to achieve the desired particle detection SNR of 10. The detection of small particles, which generate small signal levels, requires smaller detector sub-elements. The total sample volume for these particles is smaller, and hence the minimum detectable concentration is higher. As a result of these considerations the curves in Figure 17 slope downward from high concentration and small particles to low concentration and large particles. In the case of the PMT, the detector noise is so low that the particle SNR is dominated by signal shot noise. As a result, the full 5 mm × 5 mm active area can be used as a single sub-element. For the PMT, the minimum particle size that generates a shot-noise-limited SNR of 10 is about 1.4 μm. The LL CCD curve is based on a high-performance cooled Lincoln Laboratory CCD. This CCD achieves smaller particle detection than the PMT for particles less than 1.4 μm because it has a photon-detection quantum efficiency of 50%, compared to a 20% PMT photon-detection quantum efficiency. The silicon-photodiode curve rises rapidly

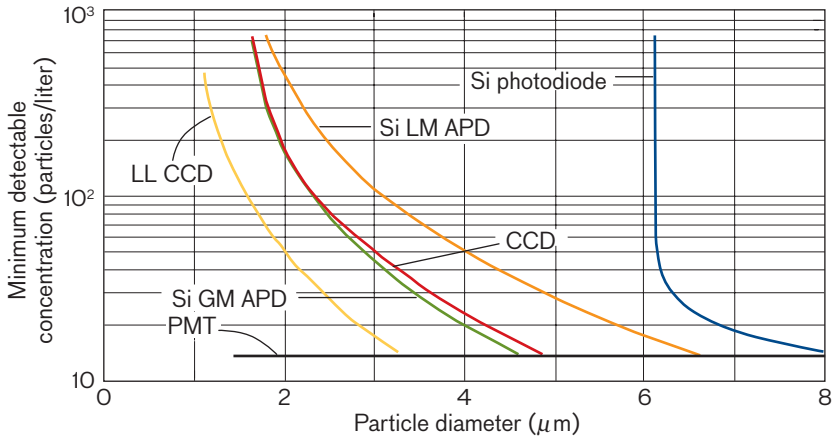

FIGURE 17. Various photodetector types exhibit different performance levels for the detection of individual biological aerosol particles. Si LM APD is a silicon linear-mode avalanche photodiode, and Si GM APD is a Geiger mode avalanche photomultiplier. LL CCD is a Laboratory-developed charge-coupled device. The baseline detector PMT is a photomultiplier tube. For this experiment, *Bg* particles were excited with a 340 nm source, the selected SNR was 10, and the total detector area was 5 mm × 5 mm.

for particles less than about 6 μm because at that point the noise is dominated by a fixed level of read-out amplifier noise. Therefore, making the silicon detector sub-elements smaller does not improve its ability to see particles smaller than 6 μm.

Light Sources

Potential sources for illumination of a particle in the sample volume include lamps, LEDs, and lasers. Lasers have the advantages of being the brightest sources, and a laser beam can easily and efficiently be transported to the sample volume. The parasitic scattering of the laser beam from optical and nearby surfaces can be well controlled and minimized. The sample volume can also be designed to take advantage of the ability to collimate the laser beam with relatively high intensity over an extended length (many times longer than the cross-sectional dimension of the laser beam). This ability allows the sample volume to be increased without decreasing the particle illumination intensity. The relatively easy manipulation of the laser beam also allows multiple passing of the beam through the sample volume so as to increase the intensity with which particles are illuminated. In addition, for pulsed applications some laser systems can store energy and release this energy in very short pulse durations. For these laser systems, pulsed illumination of particles can greatly increase the illumination intensity and signal strengths.

The Nd:YAG laser system, operating at a wavelength 1064 nm, can generate 355 nm and 266 nm radiation through nonlinear-crystal frequency tripling and quadrupling. These wavelengths are close to the optimum wavelengths for the excitation of tryptophan and NADH, respectively (see Figure 12). Pulsed (e.g., *Q*-switched or mode-locked) operation of the Nd:YAG laser allows for more efficient generation of the UV wavelengths. It was the development of the small and robust passively *Q*-switched and frequency-converted Nd:YAG microchip lasers [36–38] at Lincoln Laboratory that allowed the initial development of BAWS.

Recently, GaN-based semiconductor lasers that operate at deep blue to ultraviolet wavelengths have become commercially available. Nichia Corporation offers sources at 408 nm, with 60 mW power and 14% efficiency, and at 375 nm, with 20 mW power and 4.7% efficiency. While these lasers are not yet available at the shorter wavelengths for excitation of bio-agents, they are electrically efficient, compact, rugged, and relatively inexpensive. Because gallium nitride has a short spontaneous-emission lifetime, energy cannot be efficiently stored and then emitted in short optical pulses.

It is possible to reach shorter wavelengths with semiconductor lasers via nonlinear harmonic conversion. For example, it should be possible to access the wavelength range of 200 nm to 400 nm by third- or fourth-harmonic conversion of a mode-locked semiconductor laser operating between 800 nm and 1000 nm [39, 40].

In spite of the many advantages of lasers for bio-agent detection, for some applications in which the system cost is a primary consideration, non-laser-based trigger sensors are being developed that utilize LEDs as the primary light source. Compared to GaN-based lasers, GaN-based LEDs can operate at shorter wavelengths. With appropriate optical designs, an LED-based biosensor can illuminate potential threat particle with sufficient intensity to generate detectable fluorescence. Significant improvements have been made in power and efficiency at wavelengths as short as 280 nm. Table 2 summarizes the performance of some commercially available LEDs.

Because there are large commercial markets for semiconductor UV optical sources (e.g., data storage, sterilization, epoxy curing), these sources are expected to become more powerful, operate at shorter wavelengths, and have longer operational lifetimes in the near future.

UV lamps (e.g., mercury lamp) are a well-developed technology and have been used in bio-agent detection systems [41]. UV lamps can achieve powers and intensities that exceed LEDs (especially 280 nm LEDs). However, these lamps are bulky compared to semiconductor sources and in the case of mercury lamps are themselves hazardous. Lamps also emit multiple wavelengths, some of them overlapping with the anticipated fluorescence bands.

Trigger Systems

Building on the knowledge base acquired through the development of BAWS, Lincoln Laboratory is developing advanced trigger systems. This effort includes the development of the Inexpensive Particulate Aerosol Sensor (IPAS) and the Bio-Agent Sensor and Trigger (BAST) for substantial reduction in trigger cost, and the development of the Rapid Agent Aerosol Detector (RAAD) for substantial improvements in trigger performance.

The IPAS is designed to be an ultralow-cost particle detector for detection of threat aerosols in indoor environments. It is based on detecting particles and measuring particle size by using forward elastic-scattering signals from particles illuminated by a continuously operating near-infrared diode laser. The IPAS detection algorithm is especially tailored to look for changes in the aerosol particle size distribution that coincide with substantial increases in particle concentration.

BAST and RAAD are good examples of the fluorescence-based technologies being developed for advanced trigger systems. In comparison to BAWS, BAST and RAAD systems—still in their early development stages—are undergoing active design changes, and each system has participated in only one scored field trial.

Bio-Agent Sensor and Trigger

The BAST development effort is aimed at substantially reducing the cost of UV fluorescence-based bio-agent triggers by over a factor of ten (e.g., from its current $50,000 to well under $5000). This cost reduction is enabled by the recent development of UV LEDs (see Table 2). Replacing UV lasers ($10,000 each) with UV LEDs ($100 each) can realize substantial cost savings. However, the use of UV LEDs is not quite as simple as direct replacement of a UV laser. Because LEDs are orders of magnitude less bright than lasers, the sensor must be redesigned to efficiently utilize the LED radiation. Figure 18 shows a photograph and optical schematic of BAST. Particles entering the BAST sample volume are illuminated by both an inexpensive 820 nm diode laser and a 365 nm LED (Table 2). There are four different measurements of the particle light emission (820 nm forward elastic scattering, 365 nm side elastic scattering, 400 to 450 nm fluorescence, and 450 to 600 nm fluorescence). An example of the photodetector signals from a single particle is shown in Figure 19. The 820 nm forward-scattering measurement detects the presence of a particle and gives a measure of the particle size. The 820 nm beam also has a diagonal obscuration going through its center. This obscuration provides a dip in the 820 nm scattering signal as the particle transits the 820 nm beam that encodes the transverse position at which the particle transits the 820 nm beam. The dip shown in Figure 19 indicates that the particle went through the center of the beam. Knowledge of where the particle went through the sample volume allows correction of the particle signal for both illumination and collection efficiency variations over the sample volume. The 365 nm induced elastic scatter and fluorescence gives additional information with which to discriminate threat and nonthreat particles. Because the 365 nm elastic-scattering cross section is much larger than the fluorescence cross section, the elastic-scattering signal has a much better SNR than the fluorescence signals.

A comparison of the relative amounts of fluorescence in the two detection bands for different particle types is shown in Figure 20. Each point in these plots represents the signal levels from a single particle. On the left, Figure 20 shows the laboratory signals for *Bg*, *Yersinia rhodei* (*Yr*), and Ov particles. The wide variation in signal levels for a given type of particle is due to illumination intensity variation and signal collection variation, depending on where the particle traverses the sample volume. On the right, Figure 20 shows field data for *Bg*, Ov, and dirt particle releases in an outside background aerosol. As

Table 2: Power and Efficiency of GaN-Based LEDs

WAVELENGTH (nm)	POWER (mW)	ACTIVE AREA (mm^2)	INTENSITY (W/cm^2)	EFFICIENCY (%)	VENDOR	MODEL NUMBER
400	10	0.3×0.3	11	9	Cree	C400MB290S0100
375	2	0.18×0.18	6.2	2.8	Nichia	NSHU550A
365	200	1×1	20	10	Nichia	NCCU033(T)
340	2	0.9×0.9	0.25	0.5	Cree	Experimental 2004
280	0.5	0.1×0.2	2.5	1.1	Sensor Electronic Technology	UVTOP280

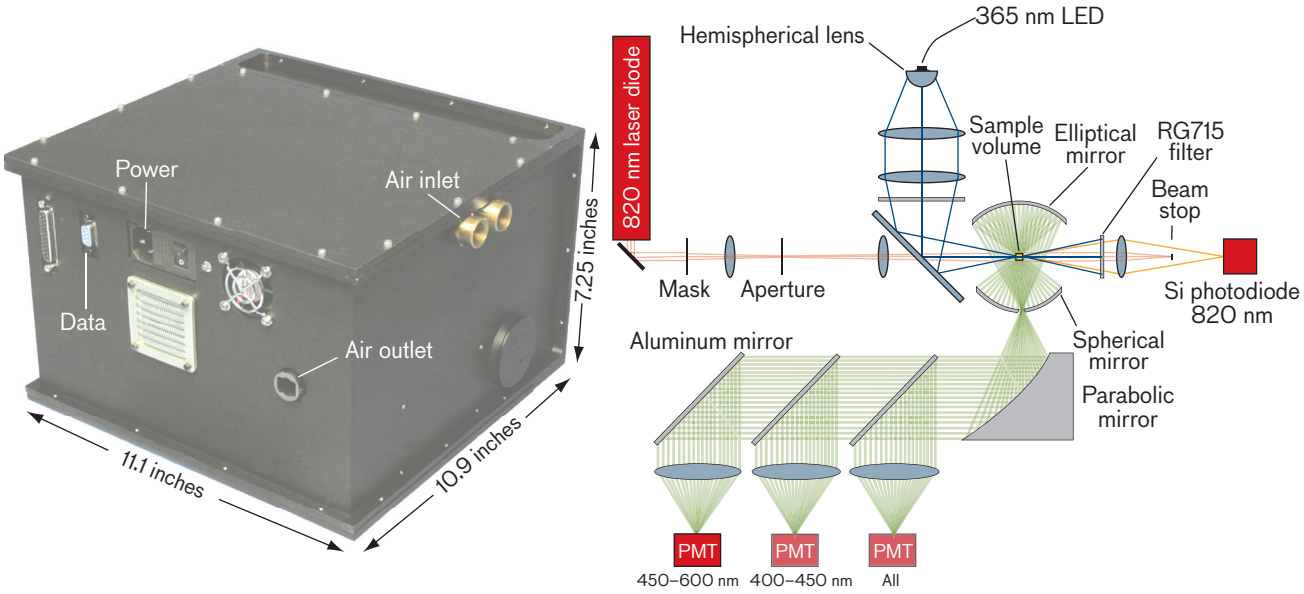

FIGURE 18. The compact, lightweight Bio-Agent Sensor and Trigger (BAST) system (0.5 cu ft, 18 lb) contains two sources, a silicon photodiode at 820 nm, and a 365 nm LED. Four detectors are set to collect 820 nm forward elastic scattering, 365 nm side elastic scattering, 400 to 450 nm fluorescence, and 450 to 600 nm fluorescence. The RG715 is a Schott optical filter glass that blocks wavelengths below 715 nm—it blocks the 365 nm source scatter and passes the 820 nm source scatter.

can be seen, *Bg* and Ov are easily discriminated from the background aerosol, but dirt has a similar signature to Ov. Another LED-based sensor is being developed that will illuminate particles with both 365 nm and 280 nm radiation to provide better particle discrimination.

Rapid Agent Aerosol Detector

The RAAD effort, a collaboration among Lincoln Laboratory, the Naval Research Laboratory, and the Army Edgewood Chemical Biological Center, is aimed at dramatically improving the performance and reliability of fluorescence-based bio-agent triggers. The performance is increased by incorporating up to fourteen measurements that are made on each particle that flows through the system. These additional measurements dramatically increase the ability to discriminate threat and nonthreat particles and therefore reduce the false-positive rate. The reliability is improved by keeping the optics clean with sheath air flow and by increasing laser lifetime by operating lasers only when particles are present in the sample volume. The RAAD is not specifically intended to be a low-manufacturing-cost instrument. Because of a lower false-positive rate and improved reliability, however, it should be a low-operating-cost instrument. This factor is important, since much of the cost associated with bioaerosol triggers comes from the cost of reacting to false triggers and from the costs associated with maintaining the sensor. The RAAD aims to dramatically reduce both of these costs.

The RAAD utilizes multiple optical sources for illumination of aerosol particles and multiple detectors for sensing the radiation emitted by the particle. The RAAD optical schematic is shown in Figure 21. The sample volume through which particles pass is illuminated by four laser beams (808 nm, 266 nm, 355 nm, and 1064 nm). The particle emission is detected by a 808-nm-sensitive

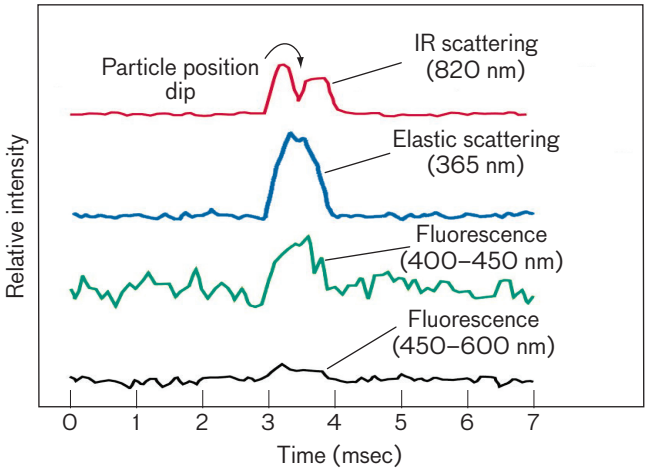

FIGURE 19. Four outputs from the BAST system appear at the same times, indicating that the data are from a single particle. Here, the raw signals are from a single 3 μm *Bg* spore.

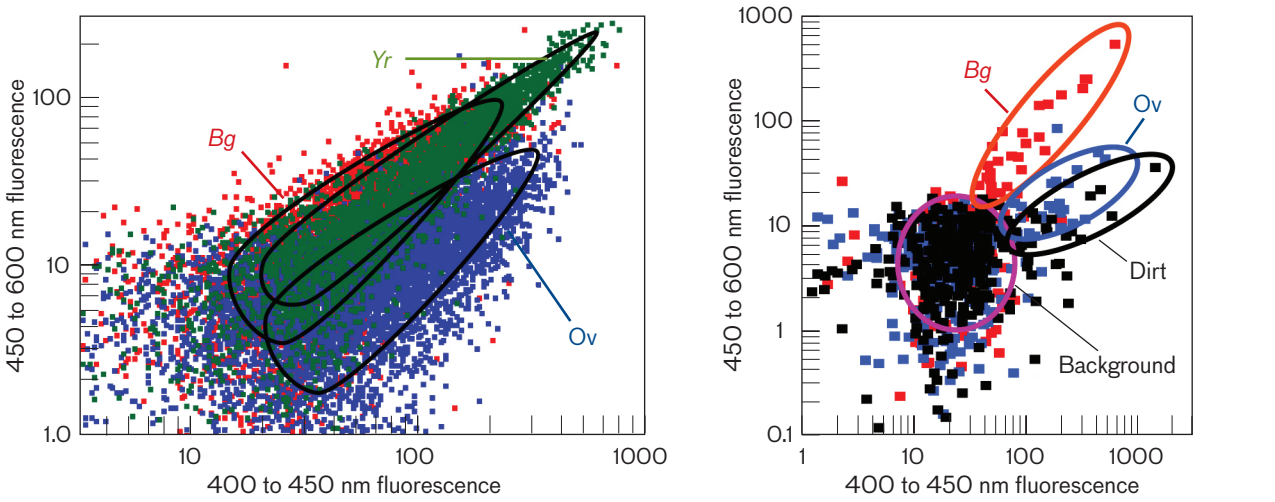

FIGURE 20. The fluorescence signals may distinguish some bio-agents from others. On the left, the three stimulants, *Bg*, *Yersinia rhodei* (*Yr*), and Ov particles, are partially overlapping. On the right, clear distinctions can be made among *Bg,* Ov, and background, but not between Ov and dirt. Each point in the graphs is a measurement of a single particle.

photomultiplier tube, a series of photomultiplier tubes for detection of UV elastic scattering and UV-induced fluorescence, and another series of photomultiplier tubes for detection of LIBS-induced plasma atomic line emission. These lasers are operated at different times as part of a staged detection system.

The RAAD is composed of three stages of detection and discrimination, as shown in Table 3. In stage 1, an aerosol particle flows into the sensor and is detected through elastic scattering from a CW 808 nm diode laser. The magnitude of the elastic-scattering signal is used to characterize the particle size, and the temporal profile of the elastic-scattering signal is used to measure the particle position [42]. As discussed later, the particle position helps normalize the other measurements for variation in illumination intensity or variation in signal collection efficiency. The stage 2 measurements are initiated for a particle with a measured diameter between 1 and 10 μm, and that is within the correct range of sample volume position. Stage 2 consists of sequentially illuminating the particle first with 266 nm laser radiation and then 355 nm laser radiation. For both of these illumination wavelengths the resulting elastic scattering and multiband fluorescence are measured. In addition, a separate detector measures the degree of polarization of the 355 nm Brewster-angle elastic scattering. As discussed earlier, Brewster-angle polarized scattering is a means to measure the particle absorption coefficient. Finally, for particles that have an elastic-scattering, fluorescence, and absorption signature similar to a bio-agent, stage 3 is initiated. Stage 3 consists of illuminating the particle with a high-energy 1064 nm laser pulse, which is sufficiently energetic and intense to induce plasma formation. Several atomic line-emission measurements are made to determine the relative elemental composition of the particle. Figure 22 shows an example of some RAAD field data that combines the

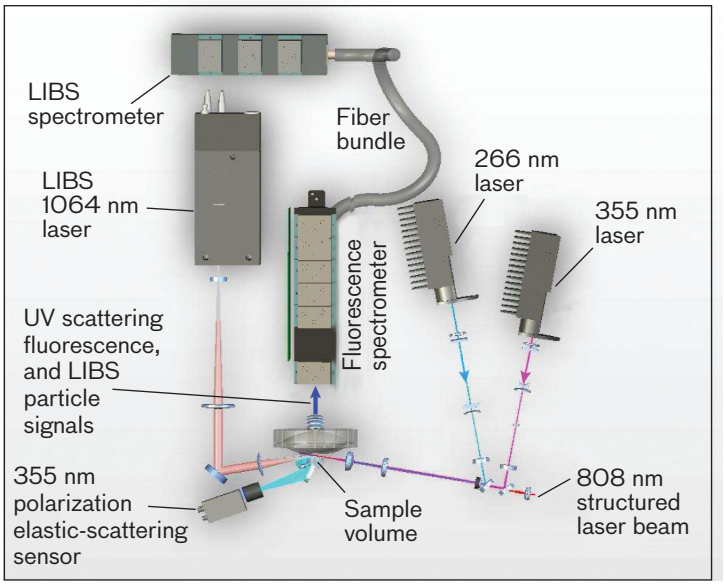

FIGURE 21. The relationship of the sample volume, lasers, and detectors is shown in this optical schematic of the RAAD breadboard unit. LIBS stands for laser-induced breakdown spectroscopy.

808 nm, 266 nm, 355 nm, and 1064 nm illumination of particles and a subset of the resulting measurements. The addition of fluorescence and LIBS data greatly improves the discrimination of agent simulants. The vertical yellow bars indicate times in which intentional interferent or agent simulants were released. At 9:45 a.m. and 4:00 p.m., unintentional dirt aerosols, distinguished by the relatively high total to fluorescent count-rate ratio, were generated. The *Yr* aerosol was distinguished by the presence of sodium (Na), as determined by LIBS.

Structured Trigger Beam

The structured trigger beam (STB) [43] is a recent development that has important implications for the design and performance of single-particle aerosol sensors. This concept was initiated in the BAST system in which it is used to find the lateral position of the particle in the sample volume. The technique has been advanced as part of the RAAD program to provide two-dimensional position and velocity information on each aerosol particle. The velocity information allows for the stage 2 and stage 3 measurements to be optimally timed to coincide with the particle being properly located for the measurements. The spatial information also allows for the correction of instrument systematic errors that broaden the particle signature.

An illustration of the STB implemented in the RAAD is depicted in Figure 23, which also shows theoretical scattering signal waveforms corresponding to the three example particle trajectories. For the purposes of this work, we assume that the particles are entrained in a laminar air flow such that their trajectories are parallel to the y-direction. The trajectories of the particles intersect four features, or beams, of the illumination pattern. These beams encode the particle's velocity along the y-axis, position along the y-axis at a given time, and position in the x-z plane.

The significance of the STB to sensor performance results in large part from the ability to use the spatial information provided by the STB to first measure the spatial dependence of the detected signal within the sensor's sample volume and then correct for any non-uniformities on a particle-by-particle basis. Figure 24 illustrates the process by which the STB is used to improve particle

Table 3: Staged Detection Architecture of the RAAD Breadboard

STAGE 1 Detection:	STAGE 2 Discrimination: multiband elastic scattering and fluorescence	STAGE 3 Discrimination: laser-induced breakdown spectroscopy
Illumination source: 808 nm laser continuous operation	Illumination sources: 266 nm pulsed laser 355 nm pulsed laser pulsed operation when particle with appropriate size is present.	Illumination source: 1064 nm pulsed laser pulsed operation when particle is present that is part of a threat-like aerosol as indicated by fluorescence measurements
Detection channel: 808 nm elastic scattering	Detection channels: 266 nm elastic scattering 355 nm elastic scattering 290 to 330 nm fluorescence 340 to 370 nm fluorescence 380 to 410 nm fluorescence 420 to 600 nm fluorescence 355 nm polarized elastic scattering	Detection channels: 285 nm magnesium emission 422 nm calcium emission 589 nm sodium emission 766 nm potassium emission
Measurements: particle size particle position	Measurements: particle relative reflectivity particle relative fluorescence spectra particle absorption	Measurements: particle atomic composition

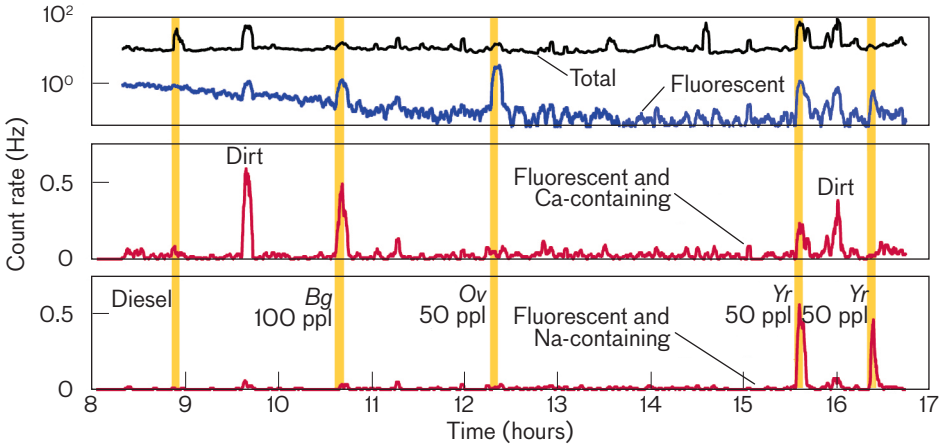

FIGURE 22. Example RAAD data show the total particle count rate and the fluorescent-particle count rate (upper graph), and the fluorescent-particle count rate combined with either calcium (middle graph) containing particles or sodium (lower graph) containing particles. The yellow vertical bars represent time intervals containing intentional aerosol releases (diesel, *Bg*, Ov, and *Yr*). The middle graph distinguishes dirt easily by combining fluorescent data and LIBS calcium measurement. Similarly, the lower graph distinguishes *Yr* well by combining the fluorescent data with LIBS analysis for sodium.

signatures. The figure on the left shows the number of particles that traversed the sensor volume as a function of x- and z-position. For these measurements, identical particles—polystyrene spheres—were used. The middle and right images of Figure 24 show the amount of signal collected in two of the detection bands of the RAAD as a function of this position. From these figures it is evident that there is significant variation of the signal collected over the sample volume. Even more significant is the fact that the spatial dependence of the elastic-scattering signal is not the same as that of the UV fluorescence.

The benefit of correcting for the spatial dependence of the instrument response function is shown in Figure 25. As can be seen in the corrected signals (the right image in Figure 25), the data are more tightly clustered, which enables better discrimination from other background particle signatures.

Trigger Algorithms

The algorithm, which is an integral part of any bio-sensor, maximizes the utility of the sensor measurements by processing raw data to determine whether an attack has occurred. There are two broad types of algorithms: static and dynamic. Static algorithms hunt for very specific properties of the sensor measurements and initiate a trigger event when certain conditions are fulfilled. An example of a static algorithm is the initiation of a trigger event whenever the sensor detects that the aerosol concentration exceeds a threshold. In contrast, dynamic algorithms compare data measured by the sensor at different times and initiate a trigger event whenever the *change* in these measurements is determined to be significant. An example of a dynamic algorithm is the initiation of a trigger event whenever the change in aerosol concentration over some time interval exceeds a threshold. Because a dynamic algorithm introduces a dependence on time, it generally offers increased discrimination ability, which is important when the other measurements do not provide enough discrimination on their own.

Dynamic trigger algorithms operate on the assumption that data sensed at a past time are free of the effect of any agent that may be affecting the current sample. The detection of an anomalous event often sets into action an identification process that determines if an attack is truly present. Because triggers are often subject to this secondary adjudication, trigger algorithms can be set to operate at higher false-positive rates than would be acceptable at the system level. For this reason the term *triggers* is used rather than *alarms*, even though the latter term is more accepted in the detection-theory literature and the mathematical analysis of trigger algorithms is conducted by using standard techniques from that field, such as the receiver operating characteristic (ROC) curve. The ROC curve is a representation of the overall system detection performance and shows the relationship between high-level performance characteristics, like probability of detection, probability of false alarm (or false-positive rate), and system sensitivity (expressed as minimum detectable attack size).

The sidebar on detection threshold shows how the setting of the threshold will affect the analysis. The probability of detection varies as the threshold is adjusted to achieve a varying probability of false alarm. At the low-

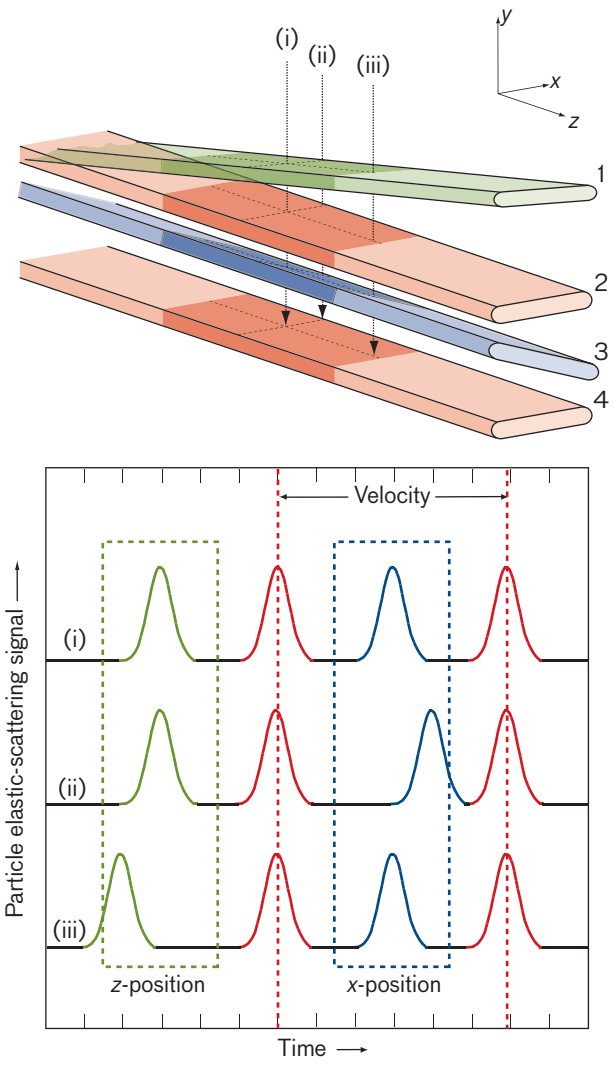

FIGURE 23. Particles moving in the *y*-direction intersect four beams of light of the structured trigger beam (STB) that is propagating in the *z*-direction. The second and fourth beams of the STB (here shown in red) are projected to have a fixed spacing for all of the particle trajectories and are used to measure particle velocity. The first and third beams (green and blue) have a variable spacing relative to the second and fourth beams and are used to encode the *z*-axis and *x*-axis position of the particle, respectively. Indicated on the illustration are three example trajectories with labels *i*, *ii*, and *iii*. Illustrations of the elastic-scattering waveforms generated by particles traveling these three trajectories with equal velocities are shown in the lower diagram. The position of the first elastic-scattering peak shifts in time to encode the particle's *z*-axis position, the third elastic-scattering peak shifts in time to encode the particle's *x*-axis position, and the second and fourth peaks encode velocity and serve as reference peaks for the particle position along the *y*-axis in time. The beams of light are all the same wavelength: the beams in this figure are colored for clarity.

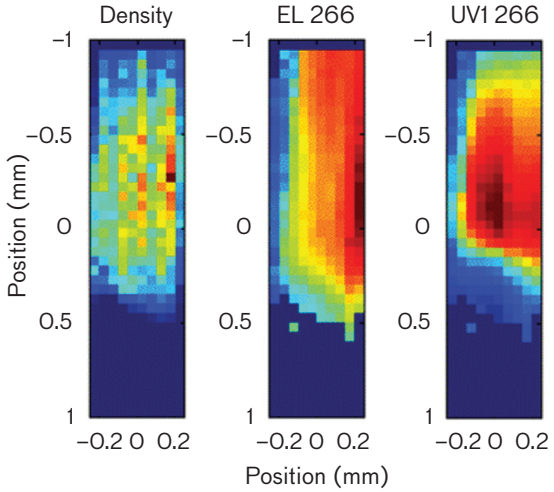

FIGURE 24. On the left is an image of the density of the particle flow, in a plane through the sample volume and at right angles to the sample flow in the RAAD instrument. The intensity of the 266 nm elastic-scattering signal (EL 266) is shown in the middle, as a function of position when measuring identical particles. The intensity of the 266 nm excited fluorescence signal (UV1 266) is shown on the right, as a function of position for the same particles. The vertical and horizontal axes have the units of millimeters. The scale is in arbitrary units with blue for zero counts and dark reds for maximum counts.

est setting of the threshold, the probability of detection is identically 100%; however, the false-alarm probability is also 100%, indicating that the alarm is triggered all the time. At the opposite extreme, the threshold is set high enough to never generate a false alarm (probability of false alarm = 0); however, this threshold is also so high that true detections are never achieved, either (probability of detection = 0). It is important to note that a ROC curve has one implicit parameter, in this case the detection threshold. Other key parameters, such as the response time, the size of the attack for which the values in the plot are valid, and the level of background clutter, are held constant or shown as overlaid curves on the same axes. Other forms of the ROC curve can be computed by holding other parameters constant, such as the probability of false alarm, and plotting, for example, probability of detection versus attack size.

Note that the concept "probability of false alarm" for a continuously operating sensor is not well defined except with respect to a time interval. Thus ROC curves showing probability of detection versus probability of false alarm are not particularly suitable for evaluating continuously operating sensors. A better and more

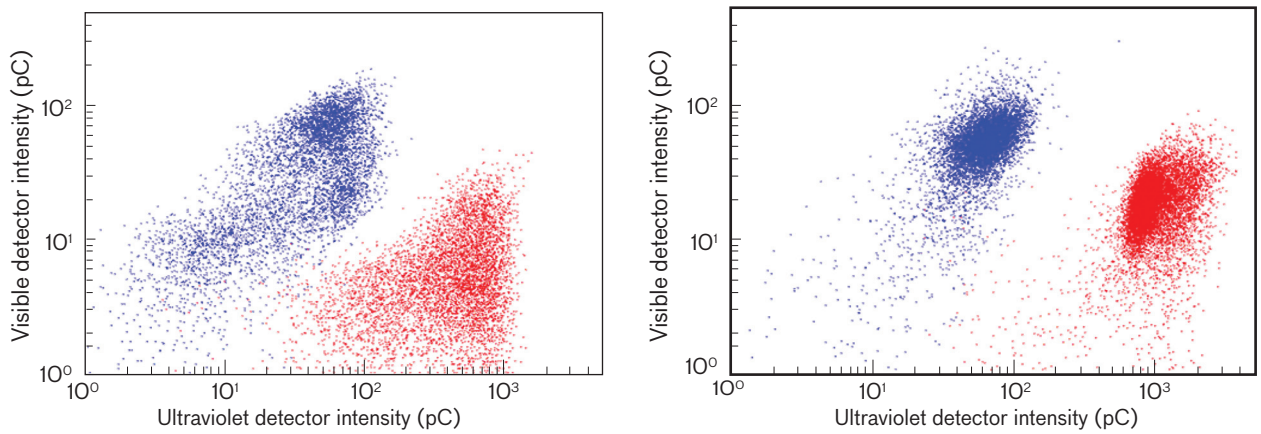

FIGURE 25. Collecting data on two fluorescent channels provides a degree of discrimination between two types of particles. The two-dimensional scatter plot on the right shows the fluorescence signatures of individual Ov particles (in red) and *Bg* particles (in blue) as collected by the RAAD instrument. The benefit of applying the correction maps derived from the data shown in Figure 24 is evident on the right. The horizontal axis represents the intensity in the 290 to 330 nm measurement channel with an excitation wavelength of 266 nm. The vertical axis represents the intensity in the 400 to 600 nm measurement channel with an excitation wavelength of 355 nm. The scale of each axis is in picoCoulombs.

understandable parameter is the false-alarm rate, expressed in terms of the number of false positives per appropriate time interval.

The ROC curve for a sensor can be used to establish an operating strategy. For example, it may be desired to maintain a constant probability of detection against a specified threat concentration. The ROC curve can be consulted to determine that this is possible only if the false-trigger rate is allowed to vary as dictated by background clutter or some other parameter uncontrollable by the system designer. In other words, operating a sensor with a constant probability of detection implies the acceptance of a false-trigger rate without constraints. If the detection probability is set unrealistically high, then the presence of high-clutter conditions will result in high false-positive rates. In practice, this is not acceptable, because high false-positive rates naturally lead to mistrust of the sensor.

An algorithm cannot work miracles. The algorithm's ability to discriminate events is only as good as the raw sensor measurements.

Given the very wide range of possible attacks and possible sensor exposure levels, the sensitivity required to detect a possible attack is actually much less well known than is the acceptable false-positive rate. Under these conditions, it makes more sense to operate the sensor in a constant-false-positive rate mode. The use of a constant-false-positive rate algorithm will result in variable sensor sensitivity at a given probability of detection, a parameter that can be estimated and reported to users. This mode of operation may be desirable as a means to maintain trust in the sensors as well as manage resources such as consumable confirmatory assays, power consumed by an adjudicating sensor, or time spent by response personnel.

Trigger-Algorithm Architecture

Biosensors like the ones described in this article measure data consisting of time-varying measurements of the optical response of air samples. The raw data are in the form of positive-valued measurements, with even nearly clean air generating a nonzero response that must be appropriately rejected to manage false-trigger rates. A simple detector may register a single value at each point in time, while more advanced sensors may collect data in multiple disjoint spectral bands to assist in background characterization so that spurious events can be more easily recognized and rejected. In either case, the trigger algorithm computes a detection statistic—a single numerical value at each point in time, and compares that value to a threshold, declaring a trigger only when the value exceeds the threshold.

Figure 26 shows a block diagram for a generic trigger algorithm, which includes the pre-processing steps required to ensure that quality data are passed to the detection algorithm. It does not specifically represent an approach in use on any sensor, but instead is meant to illustrate the high-level processes needed to implement a working algorithm.

The first algorithm step is to determine whether the present sample is indicative of the presence of a particle in the sample volume. This process can be accomplished by comparing the present signals with past signals (representative of clean air) and determining whether the difference between the present signals and past signals is significant enough to indicate that a particle is present. Any signals assessed to be related to particles are not used to update the clean air characterization. Note that this approach will not detect small particles or particles that do not generate sufficient signals. These low-signal particles will contribute to the definition of "clean air" with the effect of increasing the required signal for particle detection. Thus a particle distribution composed of many small particles—and there are always many small particles in the sample volume—will result in reduced sensitivity to very small threat particles.

Once the data have been filtered so that they are known to contain "large" particles, a second level of filtering takes place that excludes non-fluorescent particle populations from downstream processing. The reason for this step is that non-fluorescent dirt particles make up the majority of the particle loading experienced by a biosensor, and if included in the background could influence the statistics used for detection. Non-fluorescent particles can be excluded through a simple threshold that passes along only data points characterized by a minimum level

Setting Detection Thresholds

The trigger threshold depends on the probability of detection desired, but we have to watch out for the false-alarm rate.

Figure A illustrates some of the considerations involved in setting the trigger threshold. First the trigger threshold must be set high enough so that fluctuations in the clutter concentration do not generate a high false-alarm rate. Next, the trigger threshold must be set low enough to detect threat aerosol concentrations of interest. Often it is not possible to accomplish both a low false-positive rate and a high detection probability for a given threat concentration. In this case, we have to choose whether to accept an increased false-positive rate in order to achieve confident detection of the desired threat concentration, or to adjust the trigger threshold upward so as to keep

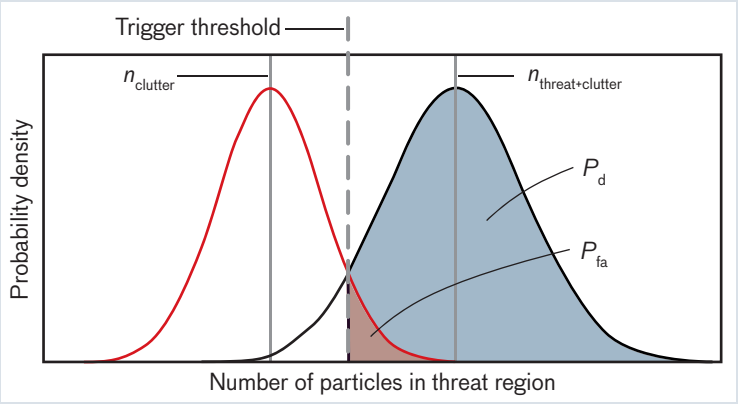

FIGURE A. Setting trigger thresholds depends on relative detection probabilities and the probability of false alarms. This plot shows the probability density for measuring a given number of particles in the threat region in a time interval *T* when clutter is present. The red curve corresponds to the probability density in the absence of any threat particles. The black curve corresponds to the probability density in the presence of threat particles. The dashed vertical line is the trigger threshold. The area under the red curve and above the trigger threshold gives the probability of a false alarm in a time period *T*. The area under the black curve and above the trigger threshold corresponds to the probability of detection of a threat concentration.

of fluorescence response to the excitation.

When the data have been filtered to include only fluorescent particles, potential threat particles are detected through the use of an anomaly detector or by checking for a specific similarity between sensed particles and elements of a threat library. When a potential threat is detected, a final decision must be made as to whether to expend a constrained confirmatory resource like a consumable immunoassay. This decision can be accomplished through the use of a persistence criterion; in other words, the confirmatory process is initiated only when the anomaly has lasted long enough that its duration serves as evidence that the anomalous population is significant enough to be sampled and properly adjudicated by the confirmatory process.

Note that the steps as described here are described as fixed algorithms; however, they may be data adaptive, for example, through the use of thresholds that are allowed to vary in response to the decisions made. For example, a threshold that is based on the distribution of recently observed clear air samples can be used to distinguish particles from clear air. This distinction is shown in the figure by the block labeled "Update clean-air characteristics filter." A similar process can be used in the fluorescent particle filter, for example, by updating the filter, as shown in the "Update non-fluorescent particle rejection filter" block. It is particularly important to impose a time-varying algorithm for threat detection, because the algorithms used for this purpose often need a good statistical characterization of the acquired background before the time when the potential threat has appeared. In the (usual) case when no threat is believed to be present, the background is constantly updated so that it does not become too old to be representative of the present time. In the

a low false-positive rate and accept a reduced sensitivity at a given detection confidence.

In the case of detecting a threat concentration C_z (z is the percent of probability detection) with a signal-to-noise ratio of $1/\sqrt{C_z \phi T}$ (i.e., no clutter) the concentration trigger threshold C_T is solely determined by the desired probability of detection:

$$C_T = C_z \left(1 - \frac{y}{\sqrt{C_z \phi T}} \right),$$

where y is given by

$$\frac{1}{\sqrt{2\pi}} \int_{-y}^{\infty} e^{x^2/2}\, dx = \frac{z}{100}.$$

Figure B shows an example plot of the concentration trigger threshold C_T as a function of the air sample rate ϕ for the detection of a threat concentration C_{98} of 25 particles per liter with a 98% probability of detection in a one-minute time interval and in the absence of clutter. Higher air sample rates allow the trigger threshold to be set closer to the desired detection concentration because more particles are sampled in the available time and the statistical uncertainty in the measured concentration is reduced.

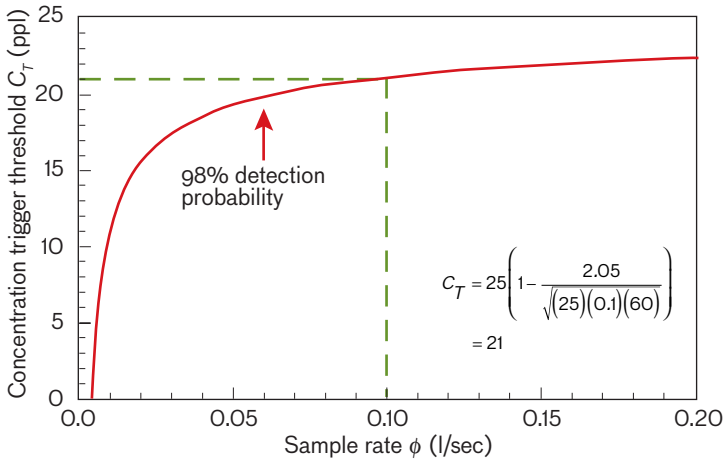

FIGURE B. A specific concentration trigger threshold is set on the basis of the detection probability z and the minimum sample rate ϕ. Here, the threat concentration is 25 particles per liter with a probability of detection of 98% and a measurement time of one minute. If, for example, the sensor air sample rate is 0.1 liters/sec, then the concentration trigger threshold must be set to 21 particles per liter in order to obtain a 98% probability of detecting an actual threat concentration of 25 particles per liter in a one-minute interval. In this example there is no clutter.

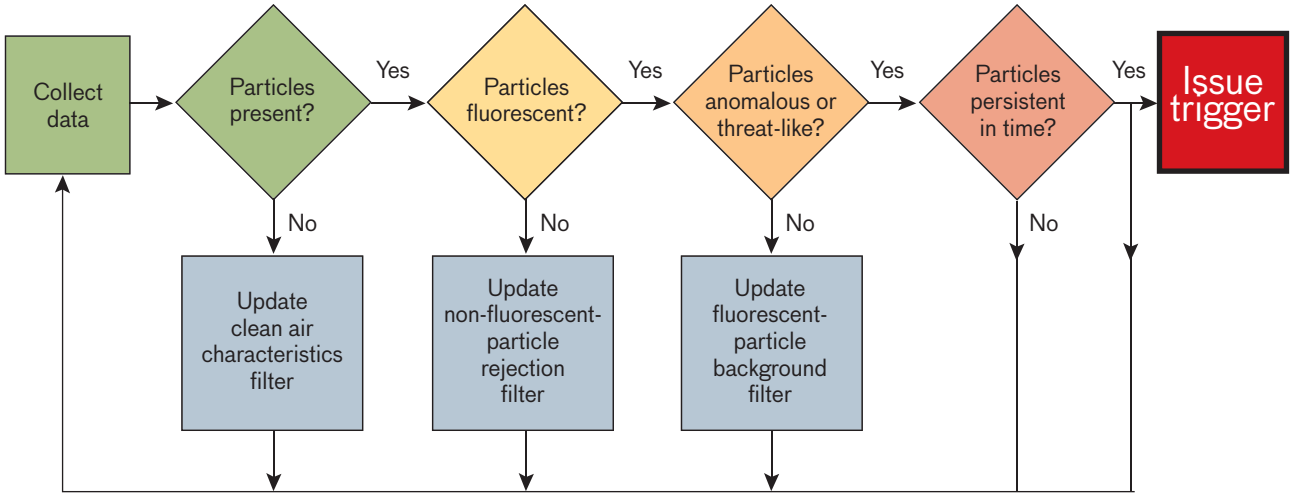

FIGURE 26. The possible implementation of a trigger algorithm follows through several decision steps, including the selection of particle-containing data, the identification of particle data with significant fluorescence, the detection of particles that are anomalous, and therefore possibly threat-like, and a persistence criterion to prevent triggering on short-term background events unlikely to be related to a bio-attack. The data collection process is typically continuous, so the algorithm may not need the feedback from each point returning to the collect data step.

times when the algorithm reports that a threat may be possible, however, the background updates are stopped to prevent the inclusion of threat particles from corrupting the background estimate.

Temporal Processing

From now on, we use the term "trigger algorithm" exclusively to describe the portion of the processing chain described in the fourth block of Figure 26, where particles are indicated as anomalous or possibly threat-like. A typical trigger algorithm divides temporal data stream into intervals, as shown in Figure 27. The sample under analysis is shown in red and denoted *Present window*, and the background interval is shown in green and denoted *Background window*. The present and background are separated by an interval shown in gray and denoted *Guard window*. The present instant is indicated by the red arrow; note that the present and background samples are in general time intervals, not single samples. The processing interval slides along in time so that the present, guard, and background windows are always at fixed times relative to the present instant.

The processing algorithm considers the data in the present and background windows and produces a single value at each point in time—the detection statistic—which is compared with a threshold to determine if it is possible that the Present window contains a threat. This information can be gotten in two ways: by detecting a signature that specifically resembles that of a threat, or by detecting an anomaly, that is, a statistically significant difference between present and past data, regardless of the resemblance of the anomaly to any known threat. The first approach can be implemented through a classification algorithm that assigns each measurement to the nearest recognized class in the feature space in which the sensor operates. Because of the need for detailed knowledge of the signal to be detected, this approach is similar to the matched filter used in communication theory to indicate the arrival of a known signaling waveform.

In biodetection, it is not clear that the signatures of threat agents will be well enough known to make their detection contingent on a high-quality match with a library template. This unfamiliarity leads to a loss of sensitivity of unknown magnitude, because of the unknown degree of mismatch between the template and the actual threat. The second strategy, that of the anomaly detector, is the subject of the discussion here. It offers the benefit of sensitivity to threats whose signatures are not known, and it can easily be configured so that false triggers occur at a relatively constant rate. As noted above, the assurance of a constant false-trigger rate is desirable from the perspective of managing disruption to operations as well as using consumable confirmation resources. Note, however, that the use of the anomaly detector as a trigger algorithm

requires a high-accuracy confirmatory process to adjudicate triggers generated by background events.

In the timeline shown in Figure 27, the lengths of the Present, Background, and Guard windows are chosen to optimize aspects of detection performance. For example, the Present window length is chosen long enough to include a detectable number of target particles even at low levels of target concentration, yet short enough that the sensor can respond quickly and reliably to transient anomalies. The Background window must be chosen long enough to provide sufficient statistical characterization of the recent past, but short enough that it does not become stale, that is, representative of an unrepresentative background too far in the past. Finally, the Guard window should be selected narrow enough that the Background window can include enough recent past data to be relevant, but long enough to prevent a slowly rising attack from passing into and contaminating the statistics of the Background window before the attack can be detected.

Because these parameters affect the sensor's performance in ways that are interrelated, they must be set with attention paid to the sensor's intended environment, including the anticipated attack size, rise time, and duration, as well as the time over which the background can be considered statistically unchanging. Note that the window lengths need not be permanently fixed; they can in principle be set by an operator in anticipation of the operational environment. Moreover, it is an area of current research to develop adaptive algorithms to improve sensitivity and false-trigger rates and to enable sensors to reliably detect that an anomaly is over so that confirmatory activity can be ceased.

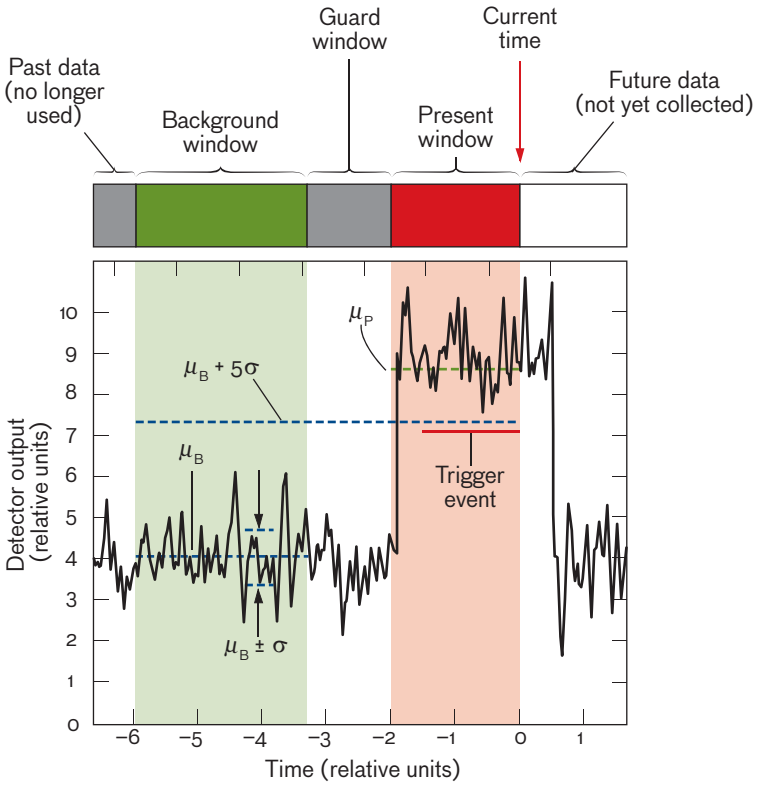

FIGURE 27. Processing of time-series data is performed with a segmentation of the data stream into present and background intervals possibly separated by a guard window. Mean and standard deviation are estimated from the background window, and a threshold is defined in terms of the background statistics. For a trigger to activate and declare an event, the threshold must be passed and the high signal rate must be persistent for a specified time.

Scalar Trigger Algorithm

For the case of a single sensor that provides data in a sequence of numerical values varying over time, a simple trigger algorithm can be defined by setting a threshold based on the mean and standard deviation of samples in the background window, and detecting when the present value exceeds that threshold. The required mean and standard deviation statistics [44] from the background can be calculated as follows:

$$\mu_B = \frac{1}{B} \sum_{i \in BW} x_i$$

and

$$\sigma_B = \sqrt{\frac{1}{B} \sum_{i \in BW} (x_i - \mu_B)^2} \,,$$

where the sums are computed over all samples in the background window, and normalized by B, the length of that interval. A trigger occurs when a sample x_i in the present window satisfies

$$x_i > \mu_B + \gamma \sigma_B \,,$$

where the value γ is here is set to achieve a false-trigger rate that accomplishes system-level goals with respect to overall false-alarm rate and the appropriate use of con-

sumable or other constrained confirmatory resources. Note that the present window can also be represented by the average value in the appropriate interval by using a similar set of equations; a single data sample is used here to simplify the discussion. The operation of this algorithm in simulated data is shown in Figure 27.

For the special case in which the background is stationary, is statistically uncorrelated, and follows a Gaussian distribution, the threshold can be set to achieve a global constant-false-alarm rate. For example, a value of $\gamma = 5$ would yield a false trigger once every 3.5 million samples, a frequency predicted from the mathematical error function. Note, however, that real background data often deviate from this ideal behavior in two ways: they generate excursions from the background distribution much more frequently than the theory would suggest, and they are correlated from sample to sample, so that one large value is frequently followed by another.

The correlation structure of the detector output is the result of the fact that both false- and true-trigger events are usually the response of the detector to a true particle cloud, which is sensed by the detector for a number of consecutive samples while the cloud is present at the detector.

The lack of Gaussianity of the data is driven by the nonstationary and inhomogeneous nature of the background aerosol. At any given time the background aerosol can be composed of multiple distinct aerosol types that change with time.

Because of these deviations from ideal statistics, we have found in practice that the threshold must be set through analysis of actual background data. Moreover, trigger events correlated in time must be anticipated by requiring consecutive samples above the threshold before declaring a trigger, for example, by assigning all consecutive triggers to a single trigger event to be adjudicated by the same confirmatory process.

Spectral Processing

When a sensor collects vector rather than scalar data (i.e., each data sample has multiple values from different spectral channels or particle size bins, for example), the scalar algorithm must be generalized through the use of linear algebraic techniques. As before, the background is characterized by its first- and second-order statistics. For the vector generalization, this implies a mean vector and covariance matrix instead of scalar mean and standard deviation values. In this case, a trigger would be generated if

$$\left(\mathbf{x}_i - \mu_N\right)^{\mathrm{T}} \left(\Sigma_B\right)^{-1} \left(\mathbf{x}_i - \mu_N\right) > \gamma,$$

where $\mathbf{x}_i$ and μ_N are the corresponding vector quantities for data and averages over the background region, and Σ_B is the covariance matrix.

For multivariate Gaussian background data analogous to that assumed in the first example, the left-hand side of this equation follows a χ^2 distribution with N degrees of freedom, where N is the dimensionality of the sample vector [45]. In principle, statistical theory can be used to set a desired false-trigger rate at a corresponding value of γ. However, as in the scalar case, anomalies are observed much more frequently than anticipated by the statistical model, and again the threshold must be set through empirical analysis of data from the intended environment.

Note that the dimensionality of the vector measurement is not necessarily the same as the true dimensionality of the signal space. For example, a sensor may record data channels whose values are all strongly correlated to particle size. If size is measured by the sensor, it can be considered jointly with the other measurements in the detection algorithm. However, if the sensor lacks a particle sizing capability, it records data that may be dominated by the effects of large particles, even if they represent a small fraction of the total population. To address this problem, some sensors, including BAWS, have implemented approaches that reduce the dimensionality of the signal space through combining channels to eliminate anticipated correlations, for example, among fluorescence bands because of their common relationship to unknown particle size [46]. Furthermore, it has been suggested that logarithmic transformation of the signals can lead to improved signal conditioning, that is, signals whose statistical distributions are more nearly normal [47].

Issues in Threshold Selection

An important design decision associated with sensor development is the selection of a threshold value for use in backgrounds that may be significantly different from the environment where the sensor is designed and tested.

For example, a sensor designed to operate in a relatively benign background may be deployed in an urban setting where the algorithm generates many more false triggers than the designers anticipated. Alternatively, a sensor designed for outdoor use may instead be used indoors to protect an airspace where the air is conditioned, filtered, and recirculated from other parts of the protected space, but nevertheless contains a high concentration of fluorescent particles arising from the human activity contained within the building. In either case, operators of the sensor may learn to ignore its alerts because they occur too frequently, thus diminishing its value.

The use of a fixed threshold may be dictated by the desire of those involved in sensor acquisition, deployment, and design to maintain a constant probability of detection against a specific threat (list of agents and specified smallest detectable attack size). In reality, sensors are deployed into environments where, even under the most severe threat conditions, an attack has been historically very unlikely. In contrast, the training and readiness of the defended personnel dictate that any sensor alarm be met with appropriate measures. Therefore, an approach to declaring alarms on the basis of a constant false-positive rate may be preferable, because it limits the frequency of alarms to a level that could be set to minimize or at least manage disruption to operational readiness.

Algorithms that operate in this mode are referred to as CFAR (constant false-alarm rate). It is important to recognize that a CFAR algorithm is implemented by using a threshold selected adaptively or in anticipation of a particular environment, and will generally not result in a constant probability of detection. In other words, a CFAR algorithm's detection capability is degraded in a challenging environment because in that setting, the detection threshold is raised to avoid excess false triggers, making it less likely that a real attack will exceed the higher threshold.

We can illustrate this property by inspection of ROC curves for the two situations discussed. It is important to recognize that a ROC curve is not an invariant characteristic of a sensor; rather, it is highly dependent on the *particular environment* the sensor operates in. It is common in analysis of communication or radar systems to overlay multiple ROC curves on a single set of axes to represent system performance at varying levels of SNR. In Figure 28, two ROC curves are shown, calculated from a simple Gaussian background simulation at two different levels of interference. The axes of this plot are those of a normal probability plot [48], and are designed to show the cumulative distribution of a Gaussian distributed random variable as a straight line. In this case, the data are exactly Gaussian because of the nature of the simulation that generated the data. However, even if they were not Gaussian, the normal probability plot would be useful in showing the values of probability close to 1 and close to 0 on the same plot.

In this example, the red curve corresponds to a more benign (higher SNR) environment and the blue curve corresponds to a more challenging (lower SNR) setting. The red curve lies above the blue curve, indicating that for all values of the probability of false alarm, the sensor is capable of higher probability of correct detection in the benign environment.

Figure 29 shows the thresholds required to achieve the probabilities of detection and false alarm shown in Figure 28. Note that thresholds that lead to equivalent detection performance in these situations do not lead to equivalent false-alarm rates (and vice versa).

Low false-alarm rate and high detection capability meet different user needs and, conversely, false alarms and missed detections impose different penalties. It is up to individual users to balance the costs and benefits of different threshold selection strategies.

Testing and Validation

The testing of aerosol triggers is a very challenging and expensive endeavor, both for the instrument developers as they build an instrument and for the U.S. government when procurement programs and the testing community need to validate a sensor's performance before a sensor transitions to full-rate production for the U.S. military. The types of tests conducted during the development life of an optical aerosol trigger are summarized in Table 4. Highlighted in this discussion are some of the challenges to testing and the infrastructure required to support the tests. In conjunction with the validation process, there are several challenges that must be addressed while performing the tests.

Safe Aerosol Protection

To test an aerosol sensor, we must first be capable of safely producing aerosols with well-known properties.

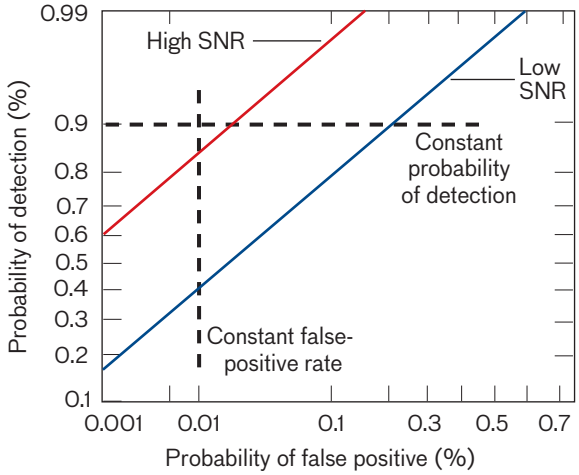

FIGURE 28. Example ROC curves for a sensor operated in two environments, one with higher and one with lower SNR, show correlated changes in probability of detection and false-positive rates. The detection algorithm threshold may be set to achieve constant probability of detection or false-positive rate. In the first case, the sensor degrades in the more challenging environment by producing more false positives and in the second case by reducing the probability of detection.

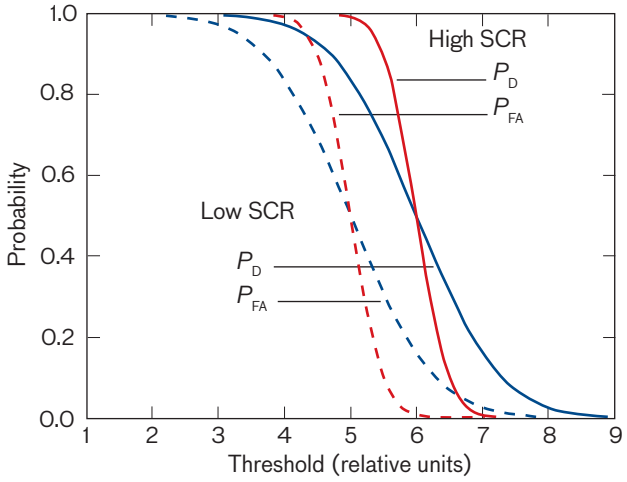

FIGURE 29. The probabilities of detection and false-alarm rate are expressed as a function of threshold for a detection algorithm operating in two different backgrounds characterized by Gaussian interference of differing signal-to-clutter ratios (SCR). Note that for achieving a desired detection rate, a threshold must be selected for each background that does not lead to constant false-alarm rate (and vice versa). P_D is the probability of detection and P_{FA} is the probability of false alarm.

Figure 30 shows a chamber for laboratory testing of aerosol sensors. Aerosols enter at the top of the chamber and are exhausted out the bottom of the chamber through a HEPA filter. To avoid possible contamination of laboratory air, users should operate the chamber at negative pressure relative to the laboratory. Because the aerosol being disseminated into the chamber is known, a simple particle counter or particle sizer instrument (e.g., the TSI Aerodynamic Particle Sizer Spectrometer) is used to measure the concentration of aerosol particles and the aerosol size distribution. In designing a safe aerosol test system it is important to filter all of the aerosols from the air before venting air from the reservoir or test equipment into the room.

The three disseminators that we find most useful are the Collison nebulizer (e.g., BGI Inc.), the Pitt

Table 4: Stages in the Testing and Validation of Optical Trigger Sensors

STAGE	PROCEDURES
Initial development	Characterize the system's response to the presence of single particles in the measurement volume and at standard aerosol-sampling rates.
	Establish the minimum detectable size of a particle.
	Catalog the signatures of simulants and interferents as recorded with the instrument.
	Produce confusion matrices.
Field testing	Test the sensor to clouds of agent simulant aerosols while operating in real environments.
	Generate ROC curves.
Operational testing	Subject the sensor to harsh physical conditions and test operational procedures with military personnel.

generator [49], and low-pressure ultrasonic spray nozzles. The Collison nebulizer is usually used for disseminating suspensions of non-soluble particles. The limitation of the Collison nebulizer is that there is little or no control over the size of particles produced. The nebulizer produces very small water droplets, ~10 microns in diameter, and therefore produces aerosols that are typically composed of single unit cells. For a sample of *Bg*, for example, the Collison nebulizer produces an aerosol with a particle size distribution consisting primarily of single spores. Figure 31 illustrates the Collison nebulizer.

The Pitt generator is used for aerosolizing powder samples such as dirt, kaolin, fungal spores, or dry *Bg* spores. The Pitt generator simply uses a diaphragm, or speaker, to vibrate a sample, thereby suspending some portion of the powder into the air. An airflow through the device carries the aerosol sample to the test setup. The Pitt generator has the benefit of producing dry aerosols that don't need to be diluted with dry air. It also preserves the original particle size distribution of the sample during dissemination, which can be a positive or negative attribute. Figure 32 illustrates the operation of the Pitt generator.

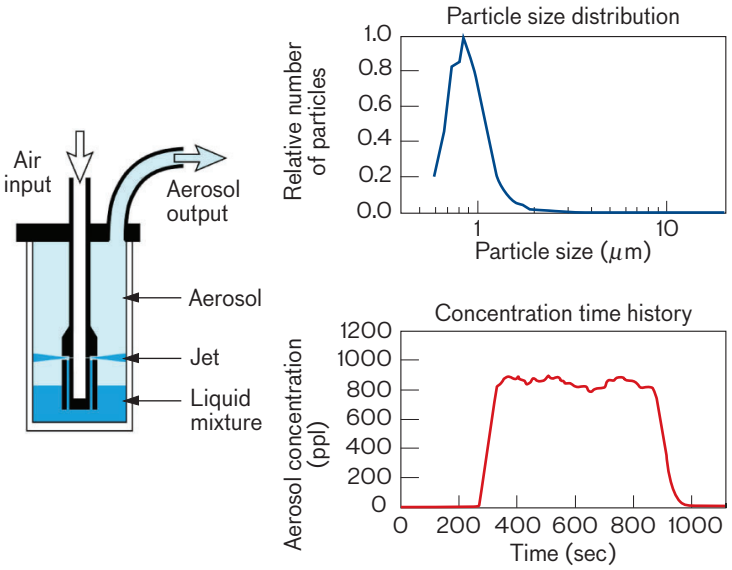

FIGURE 31. The Collison nebulizer is shown on the left. A typical particle size distribution and example of temporal control of output-concentration time history for this nebulizer are shown in the graphs.

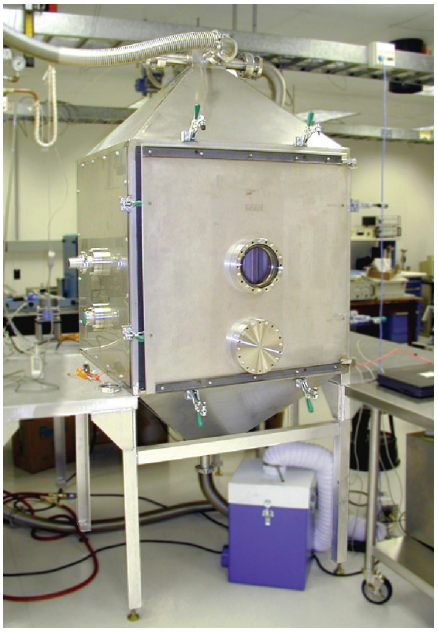

FIGURE 30. This laboratory aerosol chamber is designed to test aerosol sensors. It allows either the insertion of the sensor into the chamber or the ducting of aerosols from the chamber to the sensor. The aerosols enter the chamber at the top and are exhausted out the bottom through a HEPA filter.

One of the most useful dissemination tools is the ultrasonic spray nozzle. This tool is based on hardware from Sono-Tek Corp. for the generation of liquid droplets of dissolved or suspended material. Figure 33 shows the Sono-Tek–based Ultrasonic Disseminator System and some example particle size distributions.

Surrogate Samples

Most aerosol sensor testing is carried out by using surrogate or simulant particles in place of the actual agents. Table 5 lists some biowarfare agents and the common simulant samples that replace them for testing purposes. In addition to agent simulant samples, Table 5 also lists other materials that are aerosolized for testing, including dirt (or more specifically, Arizona road dust), kaolin, fungal spores and smuts, pollens, and calibration standards such as polystyrene spheres, either dye doped or undoped, and silica spheres.

Field Testing

Field tests are critical to the evaluation of an aerosol sensor. While signature collections during laboratory testing will usually expose the sensor to a variety of samples, the interferents used during the laboratory tests are usually

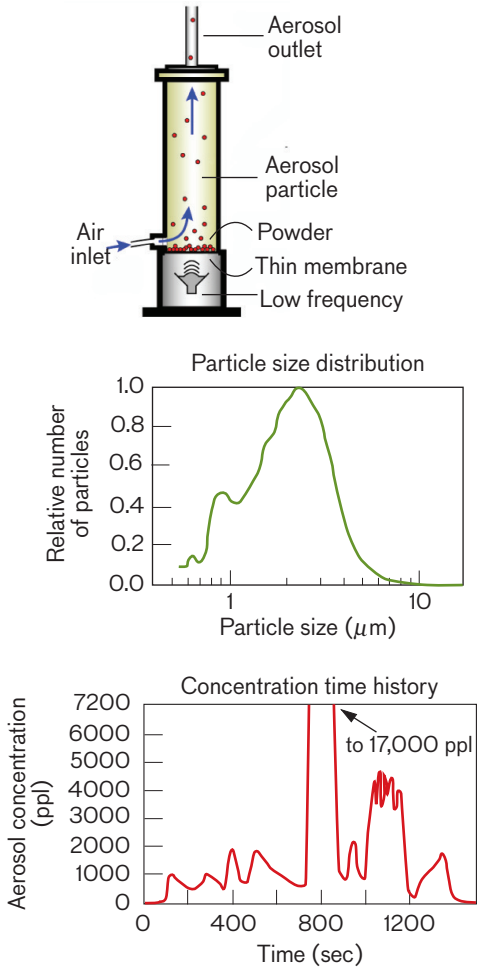

FIGURE 32. Examples of the results of the Pitt generator shown in the top photograph and diagram are the particle size distribution and output-concentration time history shown below.

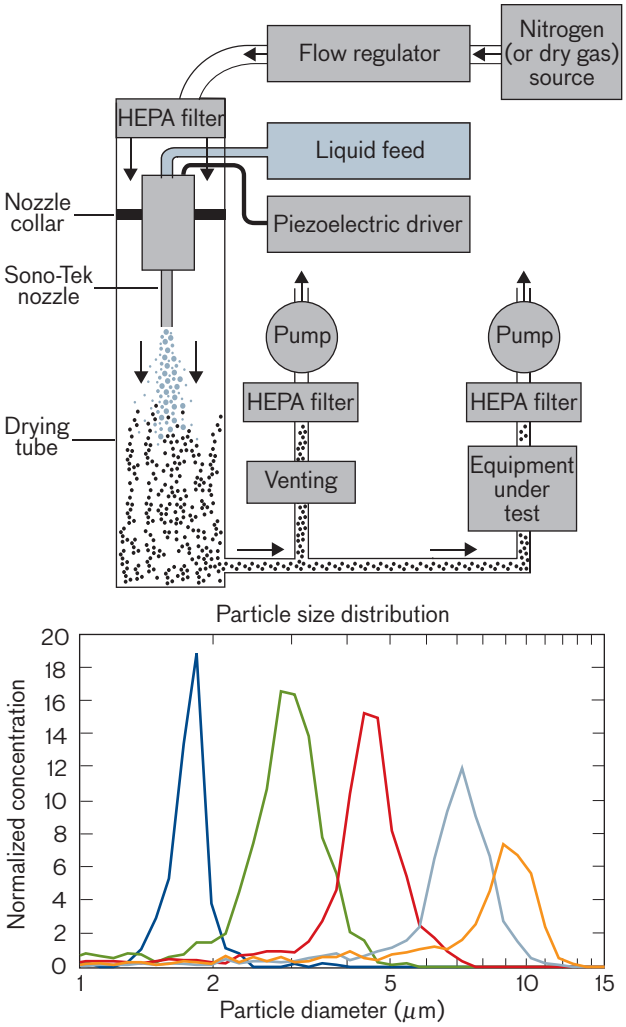

FIGURE 33. The ultrasonic aerosol dissemination system can interface directly with a trigger system under test. The piezoelectric driver nebulizes the liquid feed, and the after-filter pumps draw the nebulized sample away or through the test equipment. The graph depicts the sample size distribution for five different disseminations of *Bg* spore aerosols through the use of ultrasonic dissemination.

limited in number and selected on the basis of preconceived notions as to what materials will be problematic. Field tests can be carried out either in open-air releases or using a breeze tunnel. Open-air releases can be carried out only at a limited number of national locations, given that they involve releasing live bacteria and other materials into the air.

While testing sensors in the outdoor environment is critical to understanding their performance, there are two drawbacks to doing open-air tests. The primary problem with open air is that it is in fact difficult to hit the test grid of sensors with a controlled concentration of agent simulant. Long periods of time are spent in waiting for ideal weather conditions to release the agent simulant upwind of the sensors. When releases are made, the lack of control over the ambient conditions leads to nonuniform exposure to the agent simulants in time and over the spatial extent of the test grid. While this situation is representative of real-world releases, it is not necessarily efficient for testing. A second drawback of open-air releases is that, because of the hazards of releasing aerosols into the environment, these tests are done far from cities and population centers—areas that are heavily inhabited. As a result, anthropogenic sources of interferents are limited or nonexistent.

The solution to the challenge of outdoor testing is a breeze tunnel, which is a facility that combines the ben-

Table 5: Common Bio-Agents and Test Materials

AGENT	SIMULANT	INTERFERENTS	STANDARDS
Bacillus anthracis (Anthrax)	*Bacillus globigii*	Arizona road dust, kaolin, fungal spores, mold, smut, spores, pollens	Polystyrene spheres (dye doped or undoped), silica spheres
Yersinia pestis (Plague)	*Yersinia rhodei*		
Toxin (*Botulinum*)	Ovalbumin		
Virus (*Variola*)	MS2 phage		

efits of outdoor and indoor testing. Air from the outdoors is drawn into a tunnel, where the sensors are located. Next, disseminations of particles are superimposed on the ambient aerosol by placing a disseminator at the entrance of the tunnel. All of the air is then filtered before being exhausting into the environment. In this way the sensors are exposed to the natural aerosol background but can also be tested with agent simulants at the same time.

Environmental Testing

Ultimately, sensors need to be tested in operational environments to establish that the sensor meets the performance requirements such as sensitivity, speed of response, and false-positive rate, while operating in the harsh environments of modern battlefields. The battlefield environment introduces new stresses on the sensor that are often unforeseen during the early stages of instrument development. Most challenging to optical aerosol sensors are especially dirty environments that introduce contaminants affecting the optics or having inordinate amounts of particulates, such as smoke or dust, in the air.

Sensor developers are usually aware that battlefield conditions include dirt and smoke and are important interferents. As such, sensors are usually extensively tested during development with these materials and the sensors are designed to discriminate these from agents. In addition to being interferents for agents, however, smokes and high levels of dirt can also obscure the presence of agents from optical detection. Single-particle optical aerosol sensors inherently rely on the signal from a single agent particle located within the sample volume to be detectable above the background or noise signal that is measured in the absence of an agent particle. In the presence of very high concentrations of background aerosols, the sample volume can contain many dirt or smoke particles in addition to the agent particle. In such a situation, the signal from the agent particle may not be detectable above the signal from all of the other particles in the sample volume. Even if the signal from agents particle is detected, the measured signature may not be that of the agents. Instead, the measured signature will represent the mixture of the agent signature and that of the interferent. This representation can lead to misclassification of the agent particle and inhibit reliable detection.

The Future

In spite of years of sensor development, we remain vulnerable to a bio-agent attack that is not detected until people become sick and enter hospitals. This vulnerability persists because the sensors are too expensive, so that they are not widely enough spread to detect most possible attacks, and because the sensors have false-positive rates that are too high at the sensitivity settings that are required to detect widely dispersed agents or agents with low infectivity levels. Clearly, the development of low-cost and high-performance sensors as outlined in this article is needed. The development of low-cost sensors requires the simultaneous development of low-cost photodetectors, low-cost optical sources, and low-power particle concentrators. The development of high-performance sensors requires the development of new techniques for measuring additional particle properties that are beyond particle size, reflectivity, and fluorescence spectra and that are orthogonal to these properties.

To date, the development of trigger technologies has been separate from the development of identifier technologies. The integration of these technologies into a bio-agent sensor architecture is typically accomplished with a simple communications wire. Tighter integration should improve the performance of the overall biodetection sys-

tem. Such integration might take multiple forms. For example, the trigger could preselect threat-like particles for transmission to the identifier [50, 51]. This intelligent concentration should reduce the clutter presented to the identifier and improve its performance. In addition, the identifier could train the trigger to recognize and ignore aerosols that the trigger has previously deemed threat-like but that the identifier has determined are not threats.

The long-term utility of bio-agent sensors is greater if these sensors can provide multiple-use capability. For example, these sensors could provide much better environmental monitoring for allergens or unhealthy air than is currently available. In addition, sensors that can perform other useful functions, as well as detect bio-agents, will enjoy a better acceptance in the face of a possible decrease in the probability of an attack.

Acknowledgments

We gratefully appreciate Steven Campbell and Daniel Ripin of Lincoln Laboratory for the data they provided on fluorescent cross-sections and fluorescent excitation-emission spectra; and Xuan Eapen and Shane Tysk, also of Lincoln Laboratory, for the data they provided on aerosol particle distributions. This work was supported by the U.S. Army Research, Development and Engineering Command's Edgewood Chemical and Biological Center (David Sickenberger, Dick Smardzewski, Felix Reyes), the Joint Program Executive Office for Chemical and Biological Defense (Tim Moshier, Mark Malatesta, Dennis Card, Michael Deckert), the Defense Advanced Research Projects Agency's Microsystems Technology Office (John Carrano), and the Department of Defense's Joint Science and Technology Office for Chemical and Biological Defense (Ngai Wong). ■

REFERENCES

1. C.A. Primmerman, "Detection of Biological Agents," *Linc. Lab. J.,* vol. 12, no. 1, 2003, pp. 3–32.
2. J. Carrano, "Chemical and Biological Sensor Standards Study," Defense Advanced Research Projects Agency, Arlington, Va., Aug. 2004.
3. A.T. Young, "Rayleigh Scattering," *Phys. Today,* vol. 35, no. 1, 1982, pp. 42–48.
4. C.F. Bohren and D.R. Huffman, *Absorption and Scattering of Light by Small Particles* (Wiley & Sons, New York, 1998).
5. B. Veihelmann, M. Konert, and W. J. van der Zande, "Size Distribution of Mineral Aerosol: Using Light-Scattering Models in Laser Particle Sizing," *Appl. Opt.,* vol. 45, no. 23, 2006, pp. 6022–6029.
6. P.H. Kaye, K. Alexander-Buckley, E. Hirst, S. Saunders, and J.M. Clark, "A Real-Time Monitoring System for Airborne Particle Shape and Size Analysis," *J. Geophys. Res.*, vol. 101, no. D14, 1996, pp. 19,215–19,221.
7. E. Hirst, P.H. Kaye, V. Foot, J.M. Clark, and P.B Withers, "An Instrument for the Simultaneous Acquisition of Size, Shape, and Spectral Fluorescence Data from Single Aerosol Particles," *Proc. SPIE,* vol. 5617, 2004, pp. 416–423.
8. V.J. Foot, J. M Clark, K.L. Baxter, and N. Close, "Characterizing Single Airborne Particles by Fluorescence Emission and Spatial Analysis of Elastic Scattered Light," *Proc. SPIE,* vol. 5617, 2004, pp. 292–299.
9. K.B. Aptowicz., Y.-L. Pan, R.G. Pinnick, S.C. Hill, R.L. Tober, R.K. Chang, and B.V. Bronk, "Two-Dimensional Angular Optical Scattering Patterns of Aerosol Particles in the Mid-infrared: Measurements Designed to Obtain Particle Absorption," *Proc. SPIE,* vol. 5269, 2004, pp. 168–171.
10. K.B. Aptowicz, Y.-L. Pan, R.K. Chang, R.G. Pinnick, S.C. Hill, R.L. Tober, A. Goyal, T. Jeys, and B.V. Bronk, "Two-Dimensional Angular Optical Scattering Patterns of Microdroplets in the Mid Infrared with Strong and Weak Absorption," *Opt. Lett.,* vol. 29, no. 17, 2004, pp. 1965–1967.
11. J.R. Lakowicz, *Principles of Fluorescence Spectroscopy,* 2nd ed. (Kluwer Academic/Plenum, New York, 1999).
12. F.L. Reyes, T.H. Jeys, N.R. Newbury, C.A. Primmerman, G.S. Rowe, and A. Sanchez, "Bio-Aerosol Fluorescence Sensor," *Field Anal. Chem. Technol.,* vol. 3, no. 4–5, 1999, pp. 240–248.
13. J. Ho, " Future of Biological Aerosol Detection," *Anal. Chim. Acta,* vol. 457, no. 1, 2002, pp. 125–148.
14. J. Ho, P. Hairston, and M. Spence, "Biological Detector Performance with a 402 nm Laser Diode," Technical Report DRES TR 2000-190, Defense Research Establishment Suffield, Ralston, Alberta, Canada, 2001.
15. J. Ho, M. Spence, and P. Hairston, "Measurement of Biological Aerosol with a Fluorescent Aerodynamic Particle Sizer (FLAPS): Correlation of Optical Data with Biological Data," *Aerobiologia,* vol. 15, no. 4, 1999, pp. 281–291.
16. G.A. Luoma, P.P. Cherrier and L.A. Retfalvi, "Real-Time Warning of Biological Agent Attacks with the Canadian Integrated Biochemical Agent Detection System II (CIBADS II)," *Field Anal. Chem. Technol.,* vol. 3, no. 4–5, 1999, pp. 260–273.
17. V. Agranovski, Z. Ristovski, M. Hargreaves, P.L. Blackall, and L. Morawska, "Real-Time Measurement of Bacterial Aerosols with the UVAPS: Performance Evaluation," *J. Aerosol Sci.,* vol. 34, no. 3, 2003, pp. 301–317.
18. J.D. Eversole, J.J. Hardgrove, W.K. Cary, D.P. Choulas, and M. Seaver, "Continuous, Rapid Biological Aerosol Detection with the Use of UV Fluorescence: Outdoor Test Results," *Field Anal. Chem. Technol.,* vol. 3, no. 4–5, 1999, pp. 249-259.
19. J.D. Eversole, D. Roselle, and M.E. Seaver, "Monitoring Biological Aerosols Using UV Fluorescence," *Proc. SPIE 3533,* 1998, pp. 34–42.

20. P.J. Hargis, Jr., G.C. Tisone, J.S. Wagner, T.D. Raymond, and T.L. Downey, "Multispectral Ultraviolet Fluorescence Lidar for Environmental Monitoring," *Proc. SPIE,* vol. 2366, 1995, pp. 394–402.
21. G.W. Faris, R.A. Copeland, K. Mortelmans, and B.B. Bronk, "Spectrally Resolved Absolute Fluorescence Cross Sections for Bacillus Spores," *Appl. Opt.,* vol. 36, no. 4, 1997, pp. 958–967.
22. S.C. Hill, R.G. Pinnick, S. Niles, Y.L. Pan, S. Holler, R.K. Chang, J. Bottiger, B.T. Chen, C.S. Orr, and G. Feather, "Real-Time Measurements of Fluorescence Spectra from Single Airborne Biological Particles," *Field Anal. Chem. Technol.,* vol. 3, nos. 4–5, 1999, pp. 221–239.
23. Y.L. Pan, S. Holler, R.K. Chang, S.C. Hill, R.G. Pinnick, S. Niles, and J.R. Bottiger, "Single-Shot Fluorescence Spectra of Individual Micrometer-Sized Bioaerosols Illuminated by a 351- or a 266-nm Ultraviolet Laser," *Opt. Lett.,* vol. 24, no. 2, 1999, pp. 116–118.
24. S.V. Konev, *Fluorescence and Phosphorescence of Proteins and Nucleic Acids* (Plenum Press, New York, 1967).
25. G.W. Gould and A. Hurst, *The Bacterial Spore* (Academic Press, London, 1969).
26. J.D. Hybl, S.M. Tysk, S.R. Berry, and M.P. Jordan, "Laser-Induced Fluorescence-Cued, Laser-Induced Breakdown Spectroscopy Biological Agent Detection," *Appl. Opt.,* vol. 45, no. 34, 2006, pp. 8806–8814.
27. J.D. Hybl, G.A. Lithgow, and S.G. Buckley, "Laser-Induced Breakdown Spectroscopy Detection and Classification of Biological Aerosols," *Appl. Spectrosc.,* vol. 57, no. 10, 2003, pp. 1207–1215.
28. T. Kim, Z.G. Specht, P.S. Vary, and C.T. Lin, "Spectral Fingerprints of Bacterial Strains by Laser Induced Breakdown Spectroscopy," *J. Phys. Chem. B,* vol. 108, no. 17, 2004, pp. 5477–5482.
29. A.R. Boyain-Goitia, D.C.S. Beddows, B.C. Griffiths, and H.H. Telle, "Single-Pollen Analysis by Laser-Induced Breakdown Spectroscopy and Raman Microscopy," *Appl. Opt.,* vol. 42, no. 30, 2003, pp. 6119–6132.
30. S. Morel, N. Leone, P. Adam, and J. Amouroux, "Detection of Bacteria by Time-Resolved Laser-Induced Breakdown Spectroscopy," *Appl. Opt.,* vol. 42, no. 30, 2003, pp. 6184–6191.
31. A.C. Samuels, F.C. DeLucia, K.L. McNesby, and A.W. Miziolek, "Laser-Induced Breakdown Spectroscopy of Bacterial Spores, Molds, Pollens, and Protein: Initial Studies of Discrimination Potential," *Appl. Opt.,* vol. 42, no. 30, 2003, pp. 6205–6209.
32. J.E. Carranza, B.T. Fisher, G.D. Yoder, and D.W. Hahn, "On-Line Analysis of Ambient Air Aerosols Using Laser-Induced Breakdown Spectroscopy," *Spectrochim. Acta B,* vol. 56, no. 6, 2001, pp. 851–864.
33. M.Z. Martin, M.D. Cheng, and R.C. Martin, "Aerosol Measurement by Laser-Induced Plasma Technique: A Review," *Aerosol Sci. Technol.,* vol. 31, no. 6, 1999, pp. 409–421.
34. Hamamatsu Photonics Corporation, *Photomultiplier Tubes: Basics and Applications,* 3rd ed. (Hamamatsu City, Japan, 2006), http://sales.hamamatsu.com/assets/applications/ETD/pmt_handbook_complete.pdf.
35. V. Sivaprakasam, A. Huston, C. Scotto, and J. Eversole, "Multiple UV Wavelength Excitation and Fluorescence of Bioaerosols," *Opt. Express,* vol. 12, no. 19, 2004, pp. 4457–4466.27.
36. J. Zayhowski and C. Dill III, "Diode Pumped Passively *Q*-Switched Picosecond Microchip Lasers," *Opt. Lett.,* vol. 19, no. 18, 1994, pp. 1427–1429.
37 J.J. Zayhowski, "Diode Pumped Passively *Q*-Switched Picosecond Microchip Lasers"; "Ultraviolet Generation with Passively *Q*-Switched Microchip Lasers: Errata," *Opt. Lett.,* vol. 21, no. 19, 1996, p. 1618.
38 J.J. Zayhowski, "Passively *Q*-Switched Microchip Lasers," chap. 1 in *Solid-State Lasers and Applications,* A. Sennaroglu, ed. (CRC Press, Boca Raton, Florida, 2007), pp. 1–76.
39. L. Goldberg and D.A.V. Kliner, "Deep-UV Generation by Frequency Quadrupling of a High-Power GaAlAs Semiconductor Laser," *Opt. Lett.,* vol. 20, no. 10, 1995, pp. 1145–1147.
40. L. Goldberg and D.A.V. Kliner, "Tunable UV Generation at 286 nm by Frequency Tripling of a High-Power Mode-Locked Semiconductor Laser," *Opt. Lett.,* vol. 20, no. 15, 1995, pp. 1640–1642.
41. P.H. Kaye, W.R. Stanley, E. Hirst, E.V. Foot, K.L. Baxter, and S.J. Barrington, "Single Particle Multichannel Bio-Aerosol Fluorescence Sensor," *Opt. Express,* vol. 13, no. 10, 2005, pp. 3583–3593.
42. W.D. Herzog, S.M. Tysk, D.W. Tardiff, G.G. Cappiello, J.M. Jong, T.H. Jeys, R.H. Hoffeld, A. Sanchez, and V. Daneu, "Measurement of Aerosol-Particle Trajectories Using a Structured Laser Beam," *Appl. Opt.,* vol. 46, no. 16, 2007, pp. 3150–3155.
43. Ibid.
44. H. Stark and J. Woods, *Probability, Random Processes, and Estimation Theory for Engineers* (Prentice Hall, Englewood Cliffs, N.J., 1986).
45. A. Papoulis, *Probability, Random Variables, and Stochastic Processes* (McGraw Hill, New York, 1965).
46. Reyes, "Bio-Aerosol Fluorescence Sensor."
47. S.D. Campbell, D.P. Tremblay, F. Daver, and D. Cousins, "Multiwavelength Bioaerosol Sensor Performance Modeling," *Proc. SPIE,* vol. 5990, 2005, 59900k1–59900k13.
48. J.M. Chambers, W.S. Cleveland, and P.A. Tukey, *Graphical Methods for Data Analysis* (Duxbury Press, Boston, 1983).
49. D.A. Weyel, M. Ellakani, Y. Alarie, and M. Karol, "An Aerosol Generator for the Resuspension of Cotton Dust," *Toxicology and Applied Pharmacology,* vol. 76, no. 3, 1984, pp. 544–547.
50. K. Davitt, Y.K. Song, W.R. Patterson III, A.V. Nurmikko, Y.-L Pan, R.K. Chang, J. Han, M. Gherasimova, P.J. Cobler, P.D. Butler, and V. Palermo, "Spectroscopic Sorting of Aerosols by a Compact Sensor Employing UV LEDs," *Aerosol Sci. Technol.,* vol. 40, no. 12, 2006, 1047–1051.
51. C. Laflamme, D. Verreault, J. Ho, and C. Duchaine, "Flow Cytometry Sorting Protocol of *Bacillus* Spore Using Ultraviolet Laser and Autofluorescence as Main Sorting Criterion," *J. Fluoresc.,* vol. 16, no. 6, 2006, pp. 733–737.

ABOUT THE AUTHORS

Thomas H. Jeys is a senior staff member in the Laser Technology and Applications group. Since 1995 he has worked on the detection of aerosolized biological agents. He led the early development of the Biological Agent Warning Sensor (BAWS). He is currently investigating new biological agent detection techniques that will enable the development of low-cost biological agent sensors. He has a doctorate in atomic physics from Rice University.

William D. Herzog is a technical staff member in the Laser Technology and Applications group, where he has focused on developing technology for detecting biological aerosols. He led the early development of the Advanced Biological Agent Warning Sensor (ABAWS), a single-particle aerosol fluorescence spectrometer. He is currently the manager of the Rapid Agent Aerosol Detector (RAAD) program. He received a bachelor's degree in physics from The College of William and Mary, and a master's degree in physics and a doctorate in electrical engineering from Boston University.

John Hybl is a technical staff member in the Laser Technology and Applications group, where he has worked on applying novel optical methods to the detection of aerosolized biological agents. He has a doctorate in physical chemistry from the University of Colorado.

Richard N. Czerwinski is a staff member in the Sensor Technology and System Applications group, where his research includes detection of chemical, biological and explosive materials, and information fusion and decision support. He received a bachelor's degree in electrical engineering (cum laude) from Drexel University, and master's and doctorate degrees, also in electrical engineering, from the University of Illinois at Urbana-Champaign.

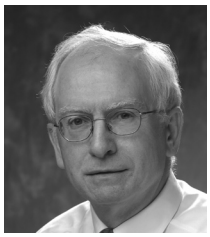

Antonio Sanchez is the leader of the Laser Technology and Applications group. He has led the development of laser systems and sensors for laser radar, infrared countermeasures, and bio-aerosol detection. He has contributed to the development of wavelength-beam-combining techniques for power and brightness scaling using semiconductor laser arrays and fiber laser arrays. He has a doctorate in physics from MIT and a bachelor's degree in physics from the University of Madrid.